A HIGH RESOLUTION PHOTON DETECTOR FOR PHENIX AT RHIC

Z.D. Cheng, J.G. Lu, X.Y. Shen, Z.P. Zheng, Y.C. Zhu
Institute of High Energy Physics, Beijing, P.R. China

A. Hershcovitch, E. Kistenev, S. Stoll, S. White, C. Woody
Brookhaven National Laboratory, Upton, NY 11973

G. David
Columbia University, Nevis Laboratories, Irvington, NY 10533

P. Dragovitsch, L.C. Dennis
Florida State University, Tallahassee, FL 32306

R. Aryaeinejad, J. Cole, M. Drigert
Idaho National Engineering Laboratory, Idaho Falls, ID 83402

R.B. Piercey
Mississippi State University, MS 39762

V.I. Kochetkov
Institute of High Energy Physics, Protvino, Russia

Yu. Gusev, V. Samsonov, A. Schetkovsky, D.M. Seliverstov, A. Vorobyov, V. Yanofsky
St. Petersburg Nuclear Physics Institute, Gatchina, Russia

R. Lacey
Chemistry Department, SUNY, Stony Brook, NY 11794

P. Braun-Munzinger, T.K. Hemmick, B. Hong, R. Hutter, M.N. Rao, S. Sedykh, J. Stachel, N. Xu, C.M. Zou
Physics Department, SUNY, Stony Brook, NY 11794

Contents

List of Figures

Chapter 1

Overview

The primary goal of this proposal is to build an electromagnetic calorimeter with excellent energy resolution and fine granularity to make precision measurements of promptly produced photons from nucleus-nucleus collisions at the Brookhaven Relativistic Heavy Ion Collider (RHIC). This detector will be incorporated into the PHENIX experiment at RHIC and should provide a unique and powerful tool to detect a new phase of matter, the quark-gluon plasma (QGP), by the measurement of prompt photon radiation.

This document is organized as follows: in Chapter 2 we will first review, after a brief introduction, what is known about prompt photon production from hadron-hadron collisions, both experimentally and theoretically. The expected photon rates from a QGP and mixed phase are then discussed with particular emphasis on where we expect clear signatures of these new phases of matter. This discussion provides the physics basics and "raison d'être " for this proposal. We also discuss how the proposed detector can be used to study soft photon production and to shed light on the polarized gluon content of the proton.

In Chapter 3 we discuss the geometry and acceptance of the proposed detector, along with the choice of technology. Chapter 4 deals with measurement strategies for the identification of prompt QGP radiation, and with a Monte Carlo evaluation of the detector performance in the RHIC environment. In Chapter 5 we describe results from prototype detector tests and our proposed calibration and monitoring scheme. The final Chapter contains the schedule and budget.

Chapter 2

Introduction and Physics Motivation

2.1 Introduction

We propose to build an electromagnetic calorimeter with excellent energy resolution and fine granularity to make a precision measurement of promptly produced photons from nucleus-nucleus collisions at RHIC. The main physics goal with the proposed detector is to observe and diagnose the quark-gluon plasma expected to be formed in such collisions. The detector will be constructed specifically to measure the spectrum of direct photons down to low values of transverse momentum (p_t) not accessible with other calorimeters.

The apparatus will be incorporated into the PHENIX experiment at RHIC [1] by replacing part of the main electromagnetic (EM) calorimeter with a finely segmented high resolution photon detector. This detector will provide a self-contained measurement of any direct photon signal. Measurements with the high resolution detector will be enhanced by the use of information from the other, larger solid angle but lower resolution, PHENIX calorimeters. In addition, results from the high resolution detector will be used to provide an independent measurement of photon signals observed in the other calorimeters at higher p_t.

We note that prompt photon production involves gluons rather than exclusively quarks as in the production of virtual photons, *i.e.* lepton pairs. Since gluon-gluon scattering cross sections are much larger than those involving quarks, gluons are expected to equilibrate much more rapidly than quarks. The measurement of the prompt photon continuum therefore provides significant information beyond what can be obtained by measuring dilepton pairs. Contrary to common belief, our studies show that the prompt photon signal from the plasma should be easier to observe than the dilepton continuum.

The proposed detector will be placed at 90° relative to the intersecting beams and will cover a sufficient portion of the solid angle for a self-contained measurement of π° and η mesons at low p_t. The precise knowledge of these meson spectra will then be used to determine the direct γ/π° ratio with a sensitivity of better than 5% down to $p_t \sim 500$ MeV/c. With this sensitivity we expect to observe plasma or mixed phase photons even if the initial temperature of the reaction zone never exceeds 240 MeV. In addition, the inclusive spectrum of photons can be measured for even lower transverse momenta (possibly on the order of a few tens of MeV/c). Using information about the spectrum of π°- and η-mesons measured in the high resolution detector as well as in the PHENIX electromagnetic calorimeter and extrapolated to low p_t one can then determine the amount of excess photons in this otherwise completely inaccessible region of phase space. The low energy detection capability of the detector will also be important to search for novel effects such as Bose-Einstein condensation of the pion gas produced in the collision, isospin fluctuations and other interesting phenomena.

The general concept and design of the high resolution photon detector is based on making use of inorganic crystal scintillators such as undoped CsI and BaF_2, which have excellent energy and time resolution, and building them into a highly granular array. We have carefully optimized the size and shape of the detector such that it can provide a self-contained measurement at low p_t, where energy resolution and granularity are of prime importance, while keeping the number of required crystals small enough to be affordable. Combined with state-of-the-art electronics and computer control the proposed detector will:

- provide a world class facility for direct photon measurements

- significantly enhance the sensitivity of the PHENIX apparatus for the detection of prompt radiation from the QGP and provide a unique capability to measure mixed phase photons to determine the phase transition temperature

- make efficient and cost-effective use of the other PHENIX detectors and infrastructure.

If built over a time-scale of three years it should be ready for day-one experiments at RHIC.

2.2 Hard Scattering Photons and QCD

The production of direct high p_t photons has been studied rather extensively in pp, pA, πA and $\bar{\rm p}$p collisions (see e.g. [2]). We present here a brief discussion of the field to summarize what is already known from hadron-hadron collisions and to point out the connections to photon production in nucleus-nucleus collisions. One of the advantages is the relative ease with which photon production can be calculated in perturbative QCD. To first order only two processes are to be considered: quark-antiquark annihilation and inverse QCD Compton scattering. As indicated in Figure 2.1, they give rise to four types of Feynman diagrams. For a given number of flavors the numers of graphs that need to be calculated for inclusive single photon production is about an order of magnitude less than say for inclusive single hadron production. Using the QCD factorization scheme, graphs a) are sensitive to the quark(antiquark) distribution function and the gluon fragmentation function while graphs b) probe the quark and gluon distribution. All graphs depend on the QCD scale parameter Λ_{QCD} or the strong coupling constant $\alpha_s(Q^2) = 12\pi/[23ln(Q^2/\Lambda^2_{QCD}]$, written here for 5 quark flavors. Due to the absence of valence antiquarks in pp and pA collisions graphs b) dominate and graphs a) enter only via the sea-quark distribution. For π^-p and $\bar{\rm p}$p collisions the annihilation diagram is dominant at large $x_t = 2p_t/\sqrt{s}$ where a valence $\bar{\rm u}$ from the projectile annihilates with a valence quark from the target. In π^+p collisions the Compton graph dominates due to the smaller electromagnetic coupling of the valence $\bar{\rm d}$. The precise ratio of the two contributions depends on the kinematic conditions.

Comparison of the above reactions among each other or to hadronic jet production provides information on gluon physics in direct photon production. While the gluon structure function can also be determined from deep-inelastic lepton scattering (DIS), there it enters as a second order process giving rise to scaling violations. Both in DIS and Drell-Yan processes the strong coupling between Λ_{QCD} and the gluon structure function makes an independent determination of the two quantities difficult. It has been shown in [2] that direct photon production has a better sensitivity to the gluon structure function.

The production rate of photons scales with $\alpha \times \alpha_s$ as compared to hadrons which scale with α_s^2, i.e. is damped by a factor α/α_s. This comparison refers however to the production of a jet and not of a single meson. The actual γ/π ratio is controlled by the fragmentation of a jet into a leading π meson. Because a photon does not fragment further its final p_t is larger than that of any other particle and γ/π increases with p_t to values significantly larger than α/α_s. It actually becomes of the order of 1 at very high p_t.

The ratio γ/π is also an experimental figure of merit. The challenge is to

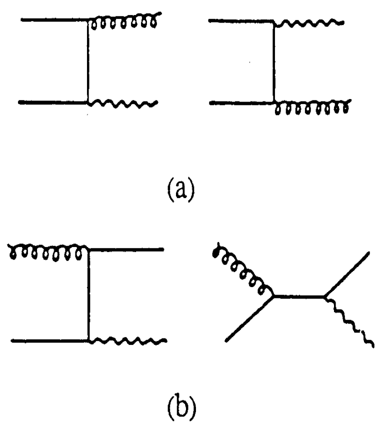

Figure 2.1: Fundamental diagrams leading to photon production: (a) $q\bar{q}$ annihilation, (b) gluon Compton scattering

single out prompt photons from a large π^0 decay background. This can either be done entirely on a statistical basis, where the π^0 (and η etc.) spectrum is reconstructed from pairs of photons. Subsequently, the inclusive photon spectrum due to this source is obtained using Monte Carlo calculations and then compared to the measured inclusive photon spectrum to search for an excess. Furthermore an enhanced sample of direct photon candidates can be obtained by imposing some kind of requirement for an isolated electromagnetic shower. Remaining background is then eliminated in the same way as described for the purely statistical method. This second method is applicable in a window in p_t determined at the low end by the size of the detector compared to the π^0 decay opening angle and the low energy detector threshold, and at the high end by the granularity of the detector and size of an electromagnetic shower as compared to the π^0 decay opening angle. For high p_t where the π^0 decay photon showers overlap in the calorimeter single photons are identified either by the shape (depth and lateral profile) of the electromagnetic shower or by the percentage of conversion in the material in front of the calorimeter (probablility that one (out of one) photon covers *vs* one out of two).

The regime where direct photon production is dominated by the Compton graphs has been studied at the ISR [3] and in fixed target experiments with protons and pions at the SPS [4] and at Fermilab [5]. Figure 2.2 summarizes the presently available date for γ/π^0 from pp collisions at $\sqrt{s} \approx$ 20-60 GeV. The ratio γ/π^0 is significantly different from zero for $p_t \geq 3$ GeV/c. As expected the ratio is found to rise with increasing p_t reaching 25 % at $p_t \approx 8$ GeV/c. Information on the $\bar{\mathrm{q}}\mathrm{q}$ annihilation term has come from fixed target

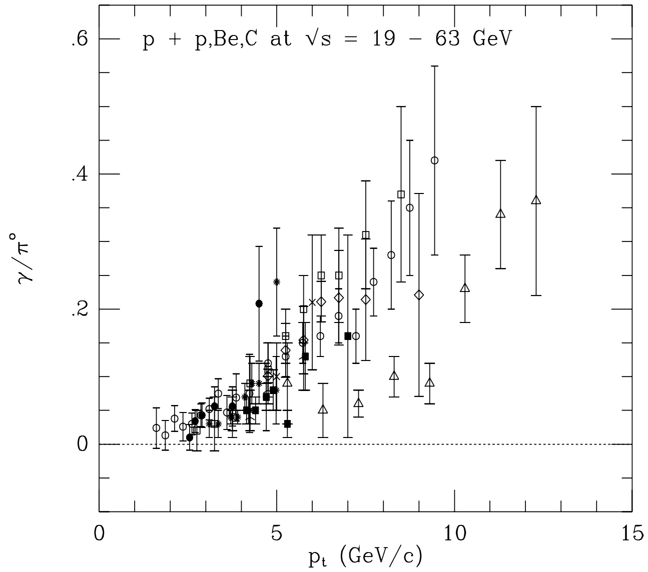

Figure 2.2: Experimental ratios γ/π^0 from pp collisions at the ISR (open symbols, [3]), Fermilab (starred symbols, [5]) and the SPS (closed symbols, [4]).

experiments using pion beams [4, 5] and from $\bar{\text{p}}$ beams [6] colliding with p beams or with an internal target for a large range of $\sqrt{s}$ = 19 GeV - 1.8 TeV and p_t = 3 - 90 GeV/c. In π^-p collisions $\gamma/\pi^0 \approx 0.4$ at $x_t = 0.5$, while in $\bar{\text{p}}$p collisions at the same x_t it starts to exceed 1. Typically at low p_t the systematic errors dominate while at high p_t statistics is the limitation. The biggest source of systematic error lies in the subtraction of remaining background from π^0 and, somewhat less importantly, η decay. It is typically of the order of 10 % of the measured signal of a few %. The uncertainty from possible hadronic contamination is up to 5-10 %. Typical absolute errors in γ/π^0 are 2-3 % at the lowest p_t where direct photons are observed. Photon cross sections have two additional sources of systematic error: the uncertainty in the p_t scale is typically 0.5-1 % which leads to a 5-10 % uncertainty in the photon cross section because of the steepness of the spectra. The uncertainty in the luminosity measurement is usually similar in magnitude. This leads to overall systematic cross section errors of 20-25 % at low p_t (3 GeV/c) and 15-17 % at $p_t \approx$ 6 GeV/c.

The current knowledge and understanding of parton distributions is summarized in [7]. Typically the nucleon quark structure functions have been obtained from DIS. Data from $\bar{\text{p}}$p$\rightarrow \gamma$X provide Λ_{QCD} and α_s using these parton distributions. The QCD scale parameter is also obtained from $\pi^- p \rightarrow \gamma$X or, even better, from the difference [$\pi^- p \rightarrow \gamma$X]-[$\pi^+ p \rightarrow \gamma$X], which isolates the annihilation graph. A systematic uncertainty is introduced by the choice of the scale Q/p_t. In order to minimize the sensitivity of the QCD calculation (typically now done at next-to-leading-order) an optimized renormalization (for α_s) and factorization (for parton distributions) scale is chosen. The most commonly used scales follow the 'principle of minimum sensitivity' and current data lead to $\Lambda_{\overline{MS}}$ ≈200 MeV with a systematic uncertainty of about 50 MeV. The gluon structure function is then obtained from the gluon dominated processes (Figure 2.1(b)). Present pp data for direct photon production favor a gluon index around 4 if the gluon distribution is parameterized as $xG(x) = A_g(1-x)^{\eta_g}$, where $x = Q^2/2M\nu$, the momentum fraction carried by a parton) for $x_t = 0.2 - 0.4$ and moderate Q^2. The systematic uncertainty is about 0.75. While inclusive photon production data for a given p_t always correspond to a range in x, measurement of the away-side jet in coincidence avoids this smearing but introduces additional systematic errors due to jet finding and definition as well as acceptance. Data on photon production in p̄p at large $\sqrt{s}$ probe smaller values of x (0.05-0.2) and large Q^2. But they are not very sensitive to the differences between soft and hard gluon distributions because scale breaking affects the two types differently. Current DIS data extend to very low x (0.01) and try to explore the x $\rightarrow$ 0 limit (constant *vs* divergent parton distributions). But the definitive answer to this question is expected from measurements of the longitudinal structure function at HERA.

The relevance of this discussion to the present proposal is twofold:

1. The production of photons in a quark-gluon plasma proceeds via the same two types of Feynman diagrams shown in Figure 2.1. The only difference to photon production in hard parton scattering is that the role of the parton distribution function is replaced by the temperature T (and its time history) giving rise to a thermal distribution. Furthermore, one also expects that the high p_t part of the photon spectrum to be measured at RHIC will be determined by initial hard parton scattering, similar to the situation in pp and pA collisions.

2. The results show what has been accomplished experimentally in hadron-hadron collisions. In particular, γ/π^0 ratios of a few % have been measured with a relative error of ≈ 20%. We note that the detector proposed here aims at similar γ/π^0 ratios, albeit for much higher particle multiplicities. This is the reason for the high granularity and excellent energy resolution of the proposed detector, which would not be required if we

only intended to study photon production in pp collisions.

A measurement of prompt photon production in pp collisions at RHIC would in itself be of interest. It would provide the data in a range of x = 0.05 to 0.15 and at moderate Q^2 where photon production is dominated by the Compton scattering graph, complementary to present collider data (UA1, UA2, CDF, D0) at the same x but for high Q^2. Extending the measurements to pA collisions would provide a unique source of information on gluon distributions in nuclei, and, hence, shed light on the very topical question of gluon shadowing. Gluon structure functions in nuclei have been determined by analysis of J/Ψ production data, although this is complicated by the contribution of processes other than gluon fusion. Initial steps to study gluon distributions in nuclei via direct photon production have been taken by the FNAL E706 collaboration [5]. At RHIC one can expect even more interesting data because of the significantly increased collision energy and because of the dramatically increased capabilities of the proposed detector.

Exciting and unique information can be obtained from reactions with polarized protons. This is discussed separately at the end of this section. Finally, making use of the results from pp and pA collisions one would obtain, in AA collisions, the connection to perturbative QCD at high p_t. This will put an enhancement at lower p_t attributed to a QGP on safe footing.

2.3 Physics Motivation for this Proposal

2.3.1 Plasma and Mixed Phase Photons

The study of real or virtual photons emitted from the anticipated QGP formed in nucleus-nucleus collisions at very high energy (RHIC,LHC) provides the only direct access to the hot initial phase of the collision, before hadronization takes place. Prompt (real) photons will originate from the (Compton) scattering of gluons and quarks. Since gluons will equilibrate very rapidly compared to quarks the prompt photon measurement leads to information not accessible with measurements of the dilepton continuum. Furthermore, as discussed in Chapter 4 in more detail, the signal/background ratio for the photon measurement is actually expected to be larger than that for the dilepton continuum. This explains our focus on real photons.

In the following we will briefly describe a scenario for the plasma and the phase transition and discuss the rate of photon production from this state of matter. Similar arguments were presented in ref.[8]. Figure 2.3 gives a

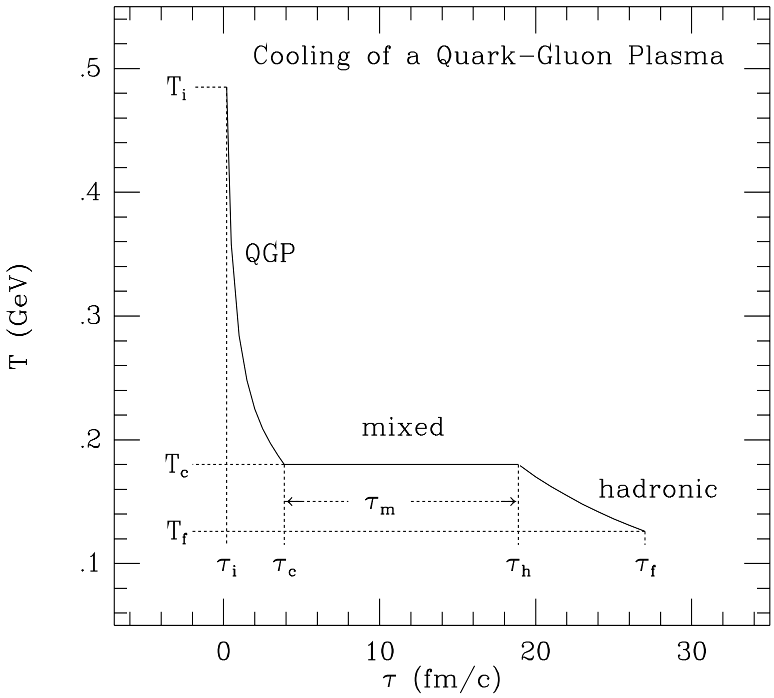

Figure 2.3: Schematic temperature development of a cooling QGP as function of the proper time.

schematic sketch of the temperature *vs* proper time development of the expansion for an intial plasma followed by a mixed and hadronic phase.

To compute photon production from a QGP we use the results of Ruuskanen [9] in a slightly schematic way in that we assume longitudinal expansion only. Following the numerical results of Bertsch et al. [10], this is probably a good approximation for the initial hot and dense phase, as well as for the mixed phase, but likely not acceptable for the purely hadronic phase. However, photon radiation from the expanding relatively low temperature hadronic phase should be small in the transverse momentum range $p_t > 0.5$ GeV/c considered here and, indeed, incorporating transverse expansion will further reduce it. We therefore have, for the following calculations, neglected the contributions from the purely hadronic phase of the collision. Under the longitudinal expansion approximation the photon transverse momentum spectrum emitted from a QGP formed in a central AA collison is calculated as

$$dN/dp_t^2 = \frac{2}{3}\alpha R_A^2 \int_{\tau_i}^{\tau_h} d\tau \tau \alpha_s T^2 (\ln(3p_t/(\pi\alpha_s T) + 1.62) K_0(p_t/T). \qquad (2.1)$$

Here, R_A is the nuclear radius, τ is the proper time of the expansion from initial time τ_i to the hadronization time τ_h, T is the temperature and K_0 is the modified Bessel function. For the strong coupling constant we use $\alpha_s = 0.4$, independent of temperature. Input parameters are the initial time τ_i, the phase transition temperature T$_c$, the duration or lifetime of the mixed phase, τ_m, and the total pion rapidity density dN_π/dy. Assuming that entropy is conserved during the collision these parameters determine the initial temperature via

$$T_i = (\frac{3.7 dN_\pi/dy}{\pi R_A^2 \tau_i a_1})^{1/3} \tag{2.2}$$

with

$$a_1 = \begin{cases} 6\pi^2/45 & \text{pion gas} \\ 3.6 \cdot 6\pi^2/45 & \text{hadron gas} \\ (32 + 21N_f) \cdot \pi^2/45 & \text{QGP, N}_f \text{ flavors} \end{cases}$$

For the following we assume N$_f$ = 2. The temperature profile is then determined from $T = T_i(\tau_i/\tau)^{1/3}$ until one reaches the mixed phase, when $T = T_c$. We also note that fixing τ_i and dN_π/dy completely determines the initial energy and entropy density ϵ_i and s_i, respectively. During the mixed phase we assume [10] that the volume fraction of QGP decreases linearly with τ. The total photon radiation from the mixed phase consists of the QGP part and the hadronic part. Following Kapusta et al. [11], one possibility is to assume that photon radiation from a hadron gas at fixed T equals that from a QGP at the same temperature. In this case the total radiation from the mixed phase only depends on T_c and τ_m and not at all on the QGP fraction.

Within this scenario we can estimate the lifetime of the mixed phase τ_m from entropy conservation. This implies that τ_m can be obtained from

$$\tau_m = \frac{s_{QGP}(T_c) - s_H(T_c)}{s_H(T_c)} \tau_c \tag{2.3}$$

with the definition of τ_c as shown in Figure 2.3 and where s_{QGP} and s_H are the QGP and hadron gas entropy densities. In order to arrive at realistic numbers we use a "realistic" hadron gas as investigated by Kataja [12]. There it is demonstrated that the hadronic phase is an equilibrized hadron gas with effective number of degrees of freedom increased by a factor of 3.6 compared to that of a pure pion gas. Typical values of τ_m are then $10 - 15$ fm/c for $dN_\pi/dy \approx 2000$ and $T_c = 0.18$ GeV. Measuring thermal photons in conjunction with the rapidity density of produced particles from nucleus-nucleus collisions at RHIC leads directly to information on the temperature history and number of degrees of freedom of the produced system. As such these experiments provide information on the equation of state. However, a hot hadronic phase with many degrees of freedom may lead to an equation of state similar to that of a QGP. This situation would be realized if the hadronic masses drop significantly in the hot hadronic matter. Photon radiation from such a state of matter could be similar to that from the QGP but under those circumstances the distinction between the two scenarios is more semantic in nature. Clearly if no QGP ever is formed and the degeneracy does not drastically increase, the initial temperature will be very high and radiation from this hypothetical system should be quite distinct from any plasma scenarios.

To put results for the photon production cross sections from the QGP into perspective one has to compare the photon rates to those of π_0 mesons produced at the same transverse momentum p_t. The ratio $N_\gamma(p_t)/N_{\pi^0}(p_t) \equiv \gamma/\pi^0$ provides a generally accepted [8] measure of the difficulty of a direct photon experiment (see also the discussion in the previous section). If $\gamma/\pi^0 < 0.01$, the measurement is extremely difficult, while for $\gamma/\pi^0 > 0.2$ the measurement is relatively straightforward. Note that this ratio not only depends on the photon production cross section but also on the pion multiplicity and the exact shape of the pion p_t spectrum. To estimate γ/π^0 values we now proceed to a parameterization of the shape of the π^0 spectrum expected for AA collisions at RHIC. Following UA1 [13] we write the spectral distribution for inclusive π^0 production in AA collisions as

$$dN_{\pi^0}/dp_t^2 = A^{1.05} r_s \exp(-m_t/T_f) + A^{4/3} r_h (p_0/(p_0+p_t))^n \exp(-p^*/p_t) \quad (2.4)$$

with parameters $T_f = 0.15$ GeV, $r_h = 23$, $p_0 = 1.8$ GeV/c and n=12.14. The values for r_h, p_0, and n are set to describe the pp collision spectrum [13]. This parameterization takes account of the fact that for central AA collisions hard scattering is expected to scale as $A^{4/3}$, while low p_t production empirically scales like $A^{1.05}$. The parameter p^* determines the transition from soft to hard scattering and is set here to $p^* = 2.5$ GeV/c. We have not tried to take account of the possibility that all minijets might be strongly absorbed in the hot and dense matter. This could significantly reduce the high p_t tail in the hadron (π^0) spectra and increase the direct photon signal. The overall multiplicity scale is set by r_s ($r_s = 39$ implies $dN_\pi/dy = 1000$).

In order to be able to estimate quantitatively the photon rate expected for various scenarios of initial equilibration time and rapidity density and to obtain upper and lower bounds on the γ/π^0 ratio we have performed a number of calculations for Au+Au collisions at RHIC. Initial results of these calculations have been reported in ref. [8]. Here we present a more detailed discussion and also provide calculations for systems studied in the CERN fixed target program at $\sqrt{s} = 19.3$ GeV. The main results are:

- At relatively low transverse momenta ($0.5 < p_t < 2$ GeV/c) the photon spectrum should be dominated by radiation from the thermalized plasma, from the mixed phase, and from the initial part of the hadronic phase.

- A rather long lived mixed phase, which is expected in case of a first order phase transition, would lead to significant radiation at the critical temperature T_c.

- Depending on the initial equilibration time, lifetime of the mixed phase, and final charged particle multiplicity a signal/background ratio of $1 < \gamma/\pi^0 < 20\%$ is observed with a maximum near p_t of 1 GeV/c, generally rising towards lower transverse momenta. However, there are significant uncertainties about the shape of the hadronic p_t spectra, one of the crucial ingredients in the signal/background calculation, implying that the maximum signal/background could be anywhere in the $0.5-2$ GeV/c range.

- For fixed dN_π/dy, the QGP part of the γ/π^0 ratio scales like $1/\tau_i$ as expected from the fact that the photon rate is proportional to T_i^3.

- Photon radiation from the hadronic phase generally exceeds that from the QGP phase except for very small τ_i values.

To illustrate these points we show, in Figures 2.4- 2.9, as function of p_t, the expected photon spectra and γ/π^0 ratios for Au+Au collisions at RHIC. The total rapidity density in the calculation was $dN_\pi/dy = 1000, 1500, 2000$ and the initial equilibration time was chosen to be $\tau_i = 1$ fm/c, and $\tau_i = 0.2$ fm/c, respectively. In each figure the top panel shows the photon rate from the QGP, from the hadron gas, from direct production, and the sum. Here, the QGP component also includes direct (hard scattering) production and the radiation from the QGP fraction of the mixed phase, the hadronic component is due to the hadron gas fraction of the mixed phase. The lower panel shows the γ/π^0 ratio calculated separately for QGP and for the hadronic phase, and the sum. For all except the most optimistic scenario with $dN/dy = 2000$ and $\tau_i = 0.2$ fm/c the γ/π^0 ratio peaks near $p_t = 1$ GeV/c, at values between $5 - 15\%$. Since we expect an experimental sensitivity for γ/π^0 in the few % range (see ref. [8] and section 4) this photon rate should be experimentally observable provided one can measure down to p_t values in the $0.5-1$ GeV/c range, which is the design goal for the proposed high resolution photon detector.

Applying the same calculational approach to what can be expected for $\sqrt{s} = 19.3$ GeV, *i.e.* for the fixed target program at CERN, we have also calculated the γ/π^0 ratio expected for Pb+Pb and O+Au collisions at this lower energy. For the O+Au case the π^0 spectrum has been measured by the WA80 collaboration [14]. The measured π^0 spectrum was used as input to the calculation along with $\tau_i = 1$ fm/c. For the Pb+Pb system, the shape of the π^0 spectrum was kept unchanged from the O+Au case, but the multiplicity was changed to $dN_\pi/dy = 500$ as expected for this system. The results, shown in Figure 2.10, imply that, because of the fairly low initial temperatures ($T_i \approx 0.2$ GeV) the γ/π^0 ratio remains below 2 % at any p_t.

Table 2.1: Summary of QGP Parameters and γ/π^0 Values for Au+Au at RHIC

τ_i (fm/c)	dN/dy	T_i (GeV)	τ_m (fm/c)	$<\epsilon>$ (GeV/fm^3)	$<s>$ (1/fm^3)	γ/π^0 at 1 GeV/c	γ/π^0 at 2 GeV/c
0.2	1000	0.41	4.1	15.7	62.7	0.057	0.025
0.2	2000	0.51	8.2	39.6	125.4	0.15	0.10
0.2	3000	0.59	12.3	68.0	188.0	0.27	0.25
1.0	1000	0.24	4.1	2.8	18.0	0.045	0.01
1.0	2000	0.30	8.2	7.1	36.0	0.13	0.03
1.0	3000	0.34	12.3	12.0	54.0	0.23	0.08

A summary of the results of a series of photon rate calculations is given in Table 2.1. Energy and entropy densities are time-averaged over the first two fm/c of the systems proper time. One should note that a major uncertainty in the present calculations is the shape of the π^0 spectrum. However, we believe that our inclusion of hard scattering tails as discussed above should provide a reasonably conservative estimate.

We note that part of our calculations has been conservative in that we have used 1 fm/c for the initial equilibration time. Recent investigations [15, 16, 17] indicate that much shorter equilibration times $\tau_i \approx 0.1 - 0.2$ fm/c are possible, although apparently only the gluons are equilibrated so rapidly. Using short equilibration times significantly increases the photon signal as is demonstrated in the calculations with $\tau_i = 0.2$ fm/c, although this result should be an overestimate if the quarks are not in equilibrium at τ_i. Recent calculations in the "hot glue" approach of Shuryak *et al.* [18] nevertheless show a strongly enhanced plasma signal compared to the standard scenario, even if only gluons equilibrate very rapidly. On the other hand, new calculations of radiation from the hadronic phase show that inclusion of the A_1 meson leads also to enhanced production from the mixed and hadronic phase [19]. A comprehensive photon measurement has to cover all these possibilities. Our main goal is, therefore,

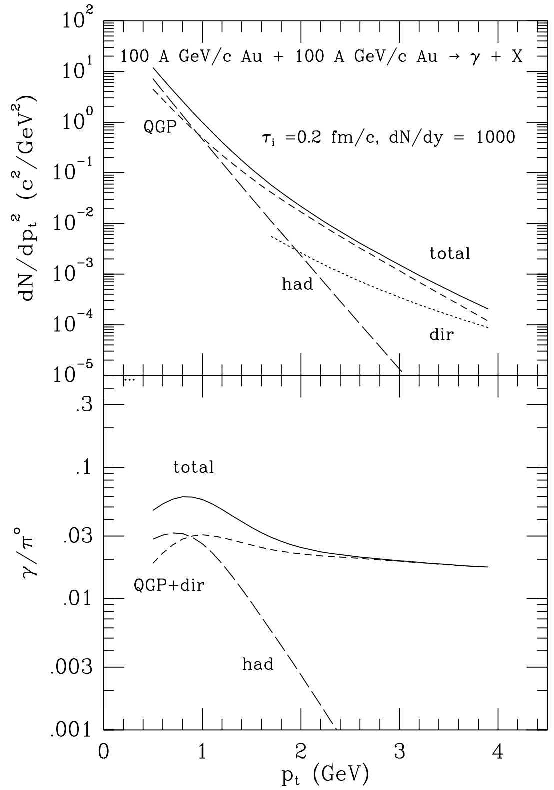

Figure 2.4: Expected π^0 and photon p_t spectra for Au + Au collisions at RHIC (top panel). The bottom panel shows the corresponding γ/π^0 ratios, separated into radiation from the QGP including hard initial scattering (short dashes) and radiation from the hadronic component of the mixed phase (long dashes). Direct production is extrapolated from pp and $\bar{\mathrm{p}}$p collision measurements using $A^{4/3}$ scaling.

to design the detector such that direct photons from the hot reaction zone can be observed under all possible scenarios. Even if, e.g., the initial temperature never exceeds 0.2 GeV and most of the radiation is emitted at temperatures near T_c we are planning to do a meaningful measurement. The excellent energy resolution, granularity and the low energy thresholds of the proposed detector will be crucial for the proposed measurement of direct photon production in the range $0.5 < p_t < 10$ GeV/c and will permit precision measurements unmatched by any other existing or proposed detector.

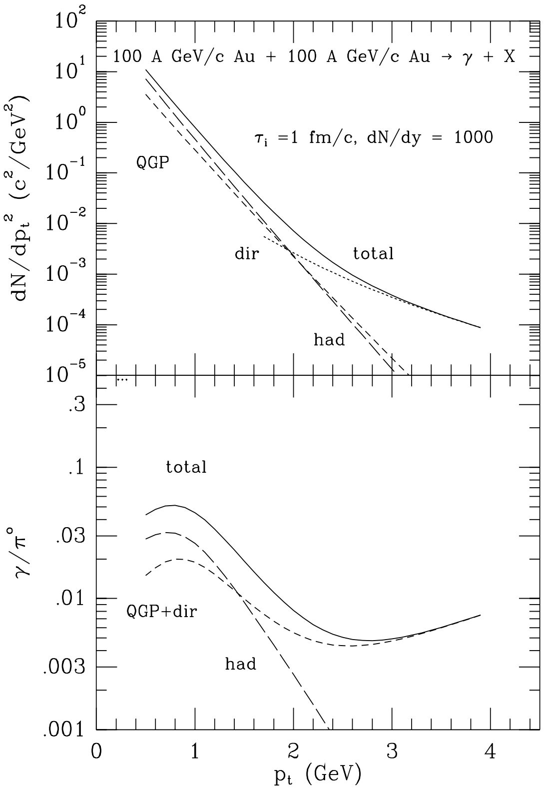

Figure 2.5: Same as Figure 2.4 for different initial conditions

2.3.2 Soft Photons and Hadronic Bremsstrahlung

While at very low p_t ($<$ 0.5 GeV/c) the actual magnitude and shape of the spectrum of photons produced by thermal radiation from the plasma is poorly known theoretically, it is generally accepted that the number of photons emitted increases rapidly with decreasing transverse momentum. At central rapidity, these photons are also produced with low energy and, below about a few hundred MeV, are considered to be "soft". In addition, low energy photons can be produced by bremsstrahlung processes [20, 21].

In the case of normal hadronic bremsstrahlung, the p_t spectrum of the bremsstrahlung photons is strongly peaked at very low p_t, and becomes a principle source of photons in the few MeV/c p_t range. These external bremsstrahlung photons will be there for any system and are due to the scattering of only the final hadrons produced in the collision (Low Theorem [22]). The size of the radiating system places limits on the energy and p_t range where this "normal" bremsstrahlung can contribute. Conversely, if the bremsstrahlung spectrum is measured, one can infer the size of the collision volume.

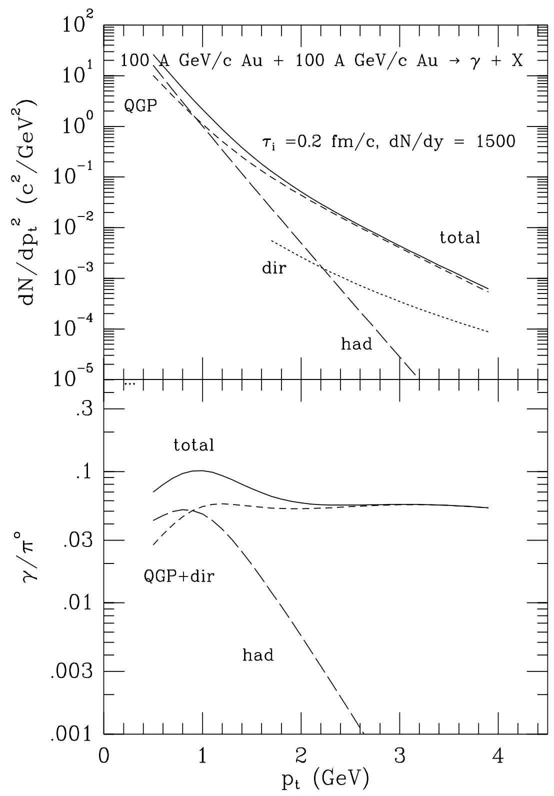

Figure 2.6: Same as Figure 2.4 for different initial conditions

These photons in fact can greatly exceed the number of photons from π^0 decays at very low p_t since the spectrum of decay photons decreases rapidly below $\sim m_{\pi^0}/2$. This is illustrated in Figure 2.11, which shows the spectrum of bremsstrahlung photons, along with those from π^0 decays, measured in pBe collisions at 450 GeV/c in the Helios experiment at CERN [23].

For photons produced by the rescattering of charged particles (mostly pions) inside a volume of dense hadronic matter, the p_t spectrum begins to rise, compared to that expected for external hadronic bremsstrahlung, above 50 MeV/c in p_t, as has been demonstrated by Shuryak [20]. The size of the effect depends on pion density and it would be very interesting to investigate this "pion-liquid" effect quantitatively. Although these photons are in the range where there is a considerable background from π^0 and other meson decays, one could isolate the rescattering component by its (quadratic) dependence on pion multiplicity, measured either in the high resolution detector itself, or in other PHENIX detectors.

Furthermore, there is the question of the existence of so-called anomalous soft photons, which have been reportedly seen in hadronic interactions [24, 25].

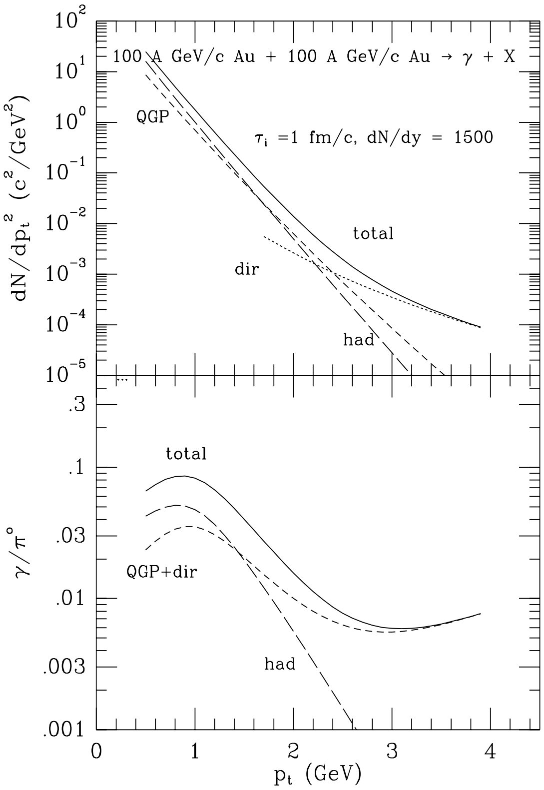

Figure 2.7: Same as Figure 2.4 for different initial conditions

These photons, if they exist, would be produced by the annihilation of soft quark-antiquark pairs produced during the collision, similar to the process which leads to the production of soft dilepton pairs [26] and would be evident in the few to tens of MeV/c p_t range. Recent results on the production of low mass electron and muon pairs have shown that most of the signal which was long believed to be anomalous can be explained by lepton pairs resulting from the Dalitz decay of the η^0 [27]. This indicates that there are no anomalous lepton pairs produced in simple hadronic collisions. There have also been experiments to look for anomalous soft photons in hadron-nucleus collsions. They have so far produced conflicting results [23, 27, 28, 29] with no convincing evidence for an anomaly. Consequently, any excess in the number of soft (virtual or real) photons which might be observed in nucleus-nucleus collisions would be all the more significant. Again, as in the case of the pion liquid photons, their rate should scale with the square of the pion multiplicity. We note that, because of their low energy, these soft photons can only be detected in the high resolution detector, making it a unique instrument at RHIC.

An intriguing possibility is that pion densities created in Au-Au collisions

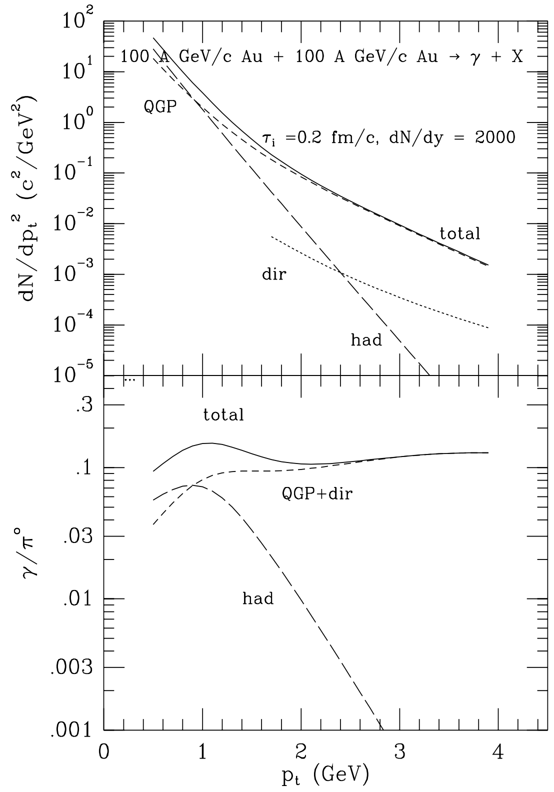

Figure 2.8: Same as Figure 2.4 for different initial conditions

at RHIC exceed the critical density for Bose-Einstein condensation. This effect has recently again been investigated by Pratt [30]. If further studies support his initial findings then one can expect rather dramatic effects for pion spectra, and in particular for spectra of π^0 mesons, where Coulomb repulsion does not come into play. Above the critical density, all π^0 mesons will collapse into an extremely low momentum state ($\Delta p \sim \hbar/R$, where R is the size of the system at freeze-out). Assuming $R \approx 10$ fm we get $\Delta p \approx 20$ MeV/c. At 90° or $y = 0$ this implies that most π^0 mesons should be produced with $p \approx p_t \approx \Delta p$, leading to a predominant source of approximately 70 MeV photons. In addition, the decay-photon background in the region $0.2 < E_\gamma < 2$ GeV would be dramatically reduced by this effect. This clearly will have strong implications for high precision studies of direct photon radiation from the hot reaction zone for those events where Bose-Einstein condensation takes place. The proposed detector would be an ideal tool to search for these events and study them in detail by identifying them via the abnormally high multiplicity of about 70 MeV photons, or more general, via the abnormal shape of the photon spectrum in the $50 - 500$ MeV range.

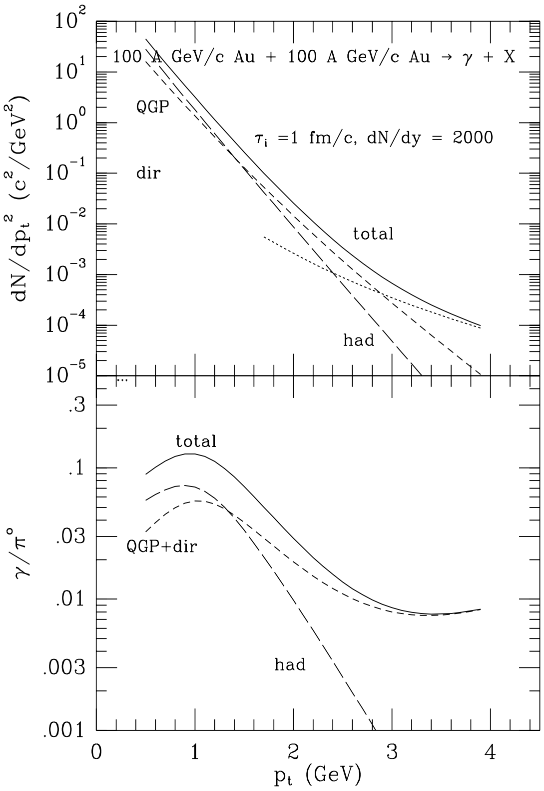

Figure 2.9: Same as Figure 2.4 for different initial conditions

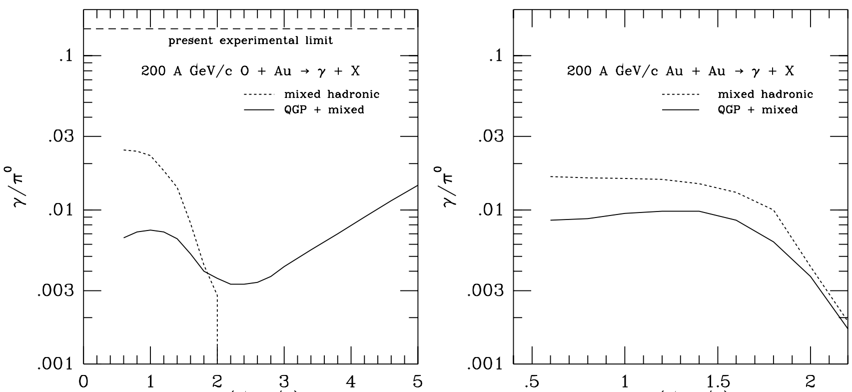

Figure 2.10: Calculated γ/π^0 ratios for O+Au and Au+Au collisions for CERN fixed target energies.

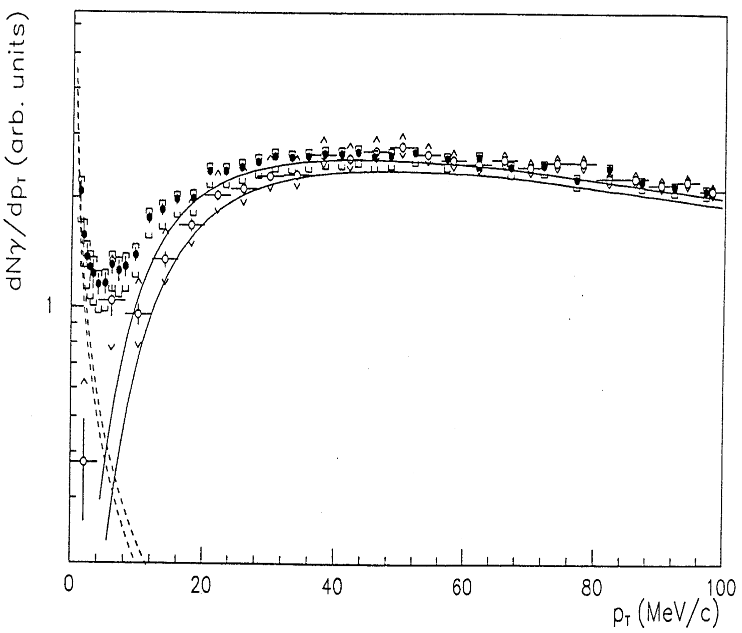

Figure 2.11: Inclusive photon spectrum measured in p+Be collisions at 450 GeV/c [23]. Open circles are from a measurement with a BaF_2 detector, closed circles are from a BGO detector. Solid lines give an estimate of the contribution to the photon spectrum from meson decays. Dashed lines give an estimate of the contribution from external bremsstrahlung.

Wilczek [31] has speculated that there might be very strong fluctuations in the ratio of neutral to charged pions due to long-range correlations near the critical point if the QGP to hadron gas phase transition is second order. Together with the charged pion results from the PHENIX tracking system, a measurement of π^0 meson spectra at low p_t with the proposed detector should be able to demonstrate these fluctuations, possibly even on an event basis.

2.3.3 The $\chi_2 \to J/\psi$ Transition

The high resolution photon detector can also be used to shed new light on the question of the spin of the proton (more precisely the "polarized gluon content" of the proton) if one can reconstruct, in $\vec{p} + \vec{p}$ collisions, the charmonium P states χ_1 and χ_2 via their J/Ψ + γ decays. The crucial idea behind this measurement is [32, 33, 34, 35] that an asymmetry measurement of the decay photon from the transition $\chi_2 \to J/\Psi + \gamma$ carries information about the helicity of the produced χ. The dominant, lowest order process for χ production at low p_t is believed to be gluon fusion: $gg \rightarrow \chi_{0,2}$ with the $gg \rightarrow \chi_1$ coupling forbidden [32]. The process of interest in the present context is χ_2 production by two gluons of the same helicity. Measurement of this process will determine the gluon distribution of the polarized proton, indicating what fraction of the proton spin is carried by the gluons. The J/Ψ will be detected in the PHENIX central detector via its e^+e^- decay, while the photon will be measured in the high resolution detector with enough resolution to separate the χ states. The $\chi_1 - J/\Psi$ and $\chi_2 - J/\Psi$ mass differences are 414 and 459 MeV. The observation of abundant χ_1 production would also be interesting since it would prove that gluon fusion is not the dominant production process. Since χ_0 is strongly suppressed, only χ_2 and χ_1 mesons have to be distinguished.

The question of what carries the spin of the proton has recently been the focus of many investigations. They were prompted by measurements of the European Muon Collaboration (EMC) of the spin asymmetry in deep inelastic scattering of longitudinally polarized muons by longitudinally polarized protons [36]. The measured asymmetry $A = (d\sigma^{\uparrow\downarrow} - d\sigma^{\uparrow\uparrow})/(d\sigma^{\uparrow\downarrow} + d\sigma^{\uparrow\uparrow})$ is sensitive to the spin-dependent gluon distribution function $g_l(x)$. Here, x is the momentum fraction carried by the gluon. From the integral $\int_0^1 g_l(x)dx$ the amount of the nucleon spin $< S_z >_{u+d}$ carried by quarks can be calculated. With data covering 98% of the integral the EMC collaboration found the surprising result that $< S_z >_{u+d} = 0.068 \pm 0.047 \pm 0.103$ or $< S_z >_{u+d+s} = 0.006 \pm 0.058 \pm 0.117$ if polarization of the strange quark sea is assumed. This implies that at most 14% of the proton spin is carried by quarks. One possible consequence of this anomaly is a large polarized gluon content of the proton [32]. This polarization is expected to be particularly large in the low x region $0.01 \leq x \leq 0.1$. The EMC data imply for the difference ΔG in the number of gluons of opposite polarization that $\Delta G = 8 \pm 2$ whereas the estimated [33] contribution to ΔG in the interval $0.1 \leq x \leq 1.0$ is about 1.5 . The planned running of polarized proton beams with $\sqrt{s} = 500$ GeV will provide the opportunity to measure polarized gg fusion in this low x region and thus probe the gluon distribution function at low x.

Assuming a luminosity of $L = 2 \cdot 10^{32}/(\mathrm{cm}^2 \cdot \mathrm{s})$ in pp collisions, a cross section of $d\sigma(J/\Psi \rightarrow e^+e^-)/dy = 10$ nb at $y = 0$, and 70% beam polarization, the J/Ψ production rate in polarized collisions is 1.4/s per unit rapidity. Using the acceptance of the proposed high resolution detector ($\Delta\Omega = 0.17$ sr, as discussed in Chapter 3), and the geometric acceptance of the electron arms in the PHENIX detector as described in the PHENIX CDR [1] we have calculated the rates of detected χ_2 mesons with a Monte Carlo simulation. To do that we have assumed that, similarly to the J/Ψ spectrum [37], the χ meson p_t

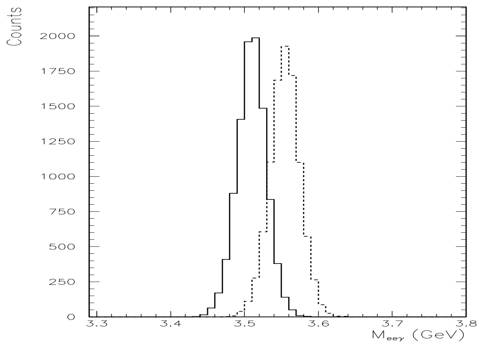

Figure 2.12: Invariant mass $M_{ee\gamma}$ for reconstruction of χ_1 and χ_2 mesons with the PHENIX apparatus.

distribution is proportional to $p_t \exp[-(p_t/p_t^0)^\beta]$ with $p_t^0 = 1.0$ GeV/c and $\beta = 5/3$. Neglecting effects of the magnetic field the probability that the decay photon is detected in the high resolution photon detector and both electrons are measured in the PHENIX apparatus is $7.1 \cdot 10^{-4}$. The branching ratio of the radiative decay is 0.135. Assuming that 40% of the J/Ψ-s are produced via χ_2 [38] one obtains a rate of $0.5 \cdot 10^{-4}$/s (≈ 0.1/hour). With full magnetic field the dielectron acceptance drops by about a factor of 3. In one month of RHIC running we therefore expect about 40 reconstructed χ_2 events. The energy resolution of the proposed detector is the crucial factor for this experiment. In the χ rest frame the decay photons are of energy 428 MeV (χ_2) and 388 MeV (χ_1). To separate them a photon resolution of $\sigma(E) = 15$ MeV or better is required, corresponding to $\sigma/E = 2\%/\sqrt{E(\mathrm{GeV})}$, the specification of the proposed detector. We have tested this with a Monte Carlo simulation and show the results in Figure 2.12.

Assuming resolutions of $\sigma/E = 2\%/\sqrt{E(\mathrm{GeV})}$ for the photon detector and $\Delta p/p^2 = 0.5\%$ for electrons detected in the PHENIX apparatus we get a mass resolution of $\Delta m \approx 20$ MeV. With this resolution the χ-peaks can be separated at the level of one standard deviation. This will not be an easy measurement but the potential physics pay-offs, as outlined above, are considerable and unique.

Chapter 3

Proposed Detector

3.1 Geometry and Acceptance

The proposed detector is rectangular and centered at $\theta = 90°$, covering $5.9°$ in polar angle θ ($\Delta\eta = 0.1$ in pseudorapidity), and $94°$ in azimuth ϕ. It is placed at a distance of 5.1 m from the intersecting beams and subtends a geometrical acceptance for photons of $\Delta\Omega = 0.17$ sr. The actual dimensions are 0.53×8.4 m^2. Since it is located at $\theta = 90°$ or $\eta = 0$, the transverse momentum is close to the total momentum, and measurements at low p_t imply detection of very low energy photons and mesons. A summary of the technical specifications is given in Table 3.1.

The proposed shape in the form of a long, thin slab is the result of an optimization of acceptance requirements, cost, and easy integration into the rest of the PHENIX detector. The kinematic acceptance for the detection of π^0 and η mesons is shown in Figure 3.1. Photon pairs from the decay of π^0 and η mesons are accepted in the proposed detector starting with very low p_t values of 140 MeV/c and 550 MeV/c, respectively. As discussed in Chapter 4, results of detailed Monte Carlo simulations imply that we can actually reconstruct π^0 and η mesons above $p_t = 0.3$ and 1.4 GeV/c, respectively.

The transverse size of the crystals is about one Molìere radius (R_M), resulting in an optimum granularity for good energy and position resolution. At a distance of 5.1 m from the intersecting beams the occupancy is kept low even in high multiplicity events. The depth is about 17.5 radiation lengths, which provides excellent energy resolution while keeping the ability to distinguish electromagnetic from hadronic energy with high efficiency. The statistical term in the energy resolution will be below $2\%/\sqrt{E(\mathrm{GeV})}$. As discussed in Chapter 6 we have actually achieved $1.8\%/\sqrt{E(\mathrm{GeV})}$) with a prototype CsI

Table 3.1: Technical Specifications of Proposed Detector

Scintillating crystals		
a) Physical Dimensions	BaF_2 Size:	$3.5 \times 3.5 \times 35$ cm^3
	Volume:	429 cm^3
	Weight:	2.10 kg
	CsI Size:	$3.5 \times 3.5 \times 32$ cm^3
	Volume:	392 cm^3
	Weight:	1.77 kg
b) Energy Resolution	Statistical Term:	$\sigma/E < 2\%/\sqrt{E(\mathrm{GeV})}$
	Noise Term:	$\sigma/E < 0.5\%/E(\mathrm{GeV})$
	Constant Term:	$\sigma/E < 1\%$
c) Position Resolution		$\delta x < (0.5 + 4.3/\sqrt{E(\mathrm{GeV})})$ mm
Mechanical Structure		
a) Module		15×15 crystals
b) Wall		8 modules
c) Calorimeter		2 walls
d) Total Number of Crystals		3,600
	BaF_2 Weight:	7,560 kg
	CsI Weight:	6,380 kg
Acceptance		
a) Detector Center	Polar Angle	$\theta = 90°$
	Pseudorapidity	$\eta = 0$
b) Coverage	Solid Angle	$\Delta\Omega = 0.17$ sr
	Azimuthal Angle	$\Delta\phi = 94°$
	Polar Angle	$\Delta\theta = 5.9°$
	Pseudorapidity	$\Delta\eta = 0.1$

detector in beam tests. This is an improvement by more than a factor of three over what can be achieved with the PHENIX Pb-glass calorimeter and a factor of four with respect to the large PHENIX Pb/scintillator EM calorimeter. The excellent position resolution (see Table 3.1) will provide an angular resolution (at 5.1 m from the interaction region) of less than 0.1° for photon energies above 200 MeV.

A figure of merit for the performance of the proposed detector is the signal to background ratio S/B for the reconstruction of π^0 mesons. Assuming that the p_t spectrum of π^0 mesons has a thermal shape (see Chapter 2) and that the photon energy resolution of the detector is $\sigma/E = \alpha/\sqrt{E}$, one can write

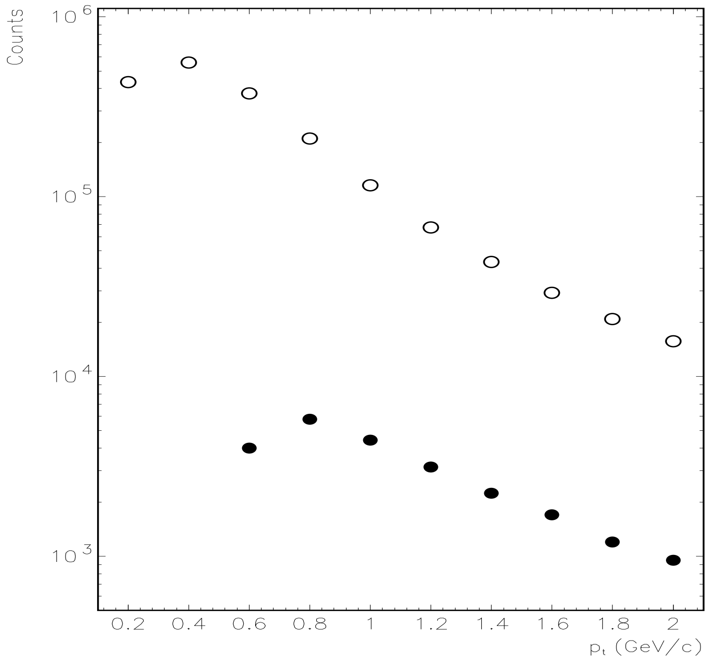

Figure 3.1: Accepted photon pairs from π^0 and η decays from 10^7 central events (about 60 hours of running time at a rate of 50/s) as function of the meson transverse momentum.

down an analytic expression for S/B under the assumption of symmetric π^0 decays, which are dominant:

$$S/B = \sqrt{2}\, 0.683\, p_t^{3/2} / (m_\pi \alpha \, dN_{\pi^0}/dy) \tag{3.1}$$

if one integrates the signal and the combinatorial background over $\pm 1\sigma$, where σ is the resolution of the π^0 mass peak. The S/B ratio is inversely proportional to dN_{π^0}/dy, *i.e.* the density of hits on the detector, and increases linearly with better π^0 mass resolution, mostly determined by the energy resolution of the detector. Note that within the above assumptions S/B is *independent* of the geometry of the detector. The above relation also indicates how much is gained by using a detector with improved energy resolution. At fixed S/B and dN_{π^0}/dy the transverse momentum corresponding to these values scales like $\alpha^{2/3}$. This implies, *e.g.* that for $dN_{\pi^0}/dy = 400$ and resolutions determined

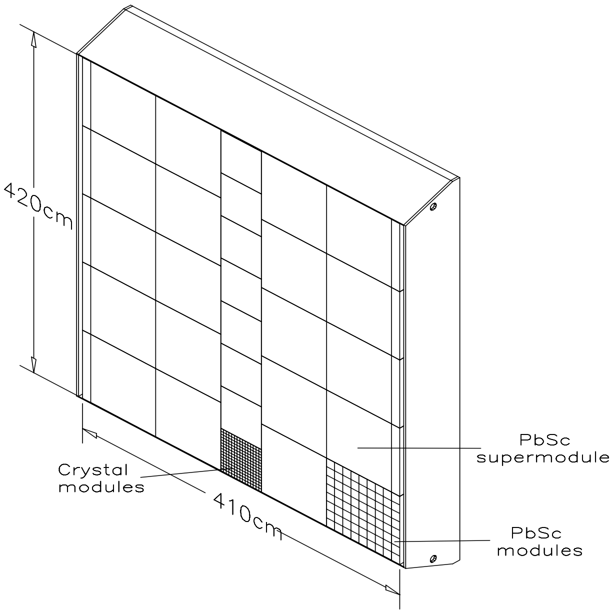

Figure 3.2: Location of the high resolution photon detector inside one of the Pb/scintillator calorimeter walls.

by α = 2% and 6%, a signal to background ratio S/B =0.3 is reached at p_t = 0.7 GeV/c and 1.6 GeV/c, respectively. This is one way to demonstrate the importance of energy resolution for the photon measurement.

For fixed cost, *i.e.* fixed detector area, we have consequently optimized the detector in the following way: the rectangular shape is chosen for detection of π^0 and η mesons at very low p_t values, the high granularity and excellent energy resolution keep S/B large and insure optimal photon reconstruction efficiency.

3.2 System Integration

The high resolution photon detector will be integrated into two walls of the PHENIX Pb/scintillator EM calorimeter. It will replace approximately 400 (5 $\times$ 80) Pb/scintillator modules in the central region of two of the calorimeter walls, as shown in Figure 3.2. The overall dimensions of the high resolution detector are 52.5 $\times$ 840 cm^2, and the detector will be divided into two walls of 52.5 $\times$ 420 cm^2. The dimensions of the crystals (3.5 $\times$ 3.5 cm^2) and of the Pb/scintillator modules (10.5 $\times$ 10.5 cm^2) are chosen such that a direct replacement can be made without modification of the surrounding support

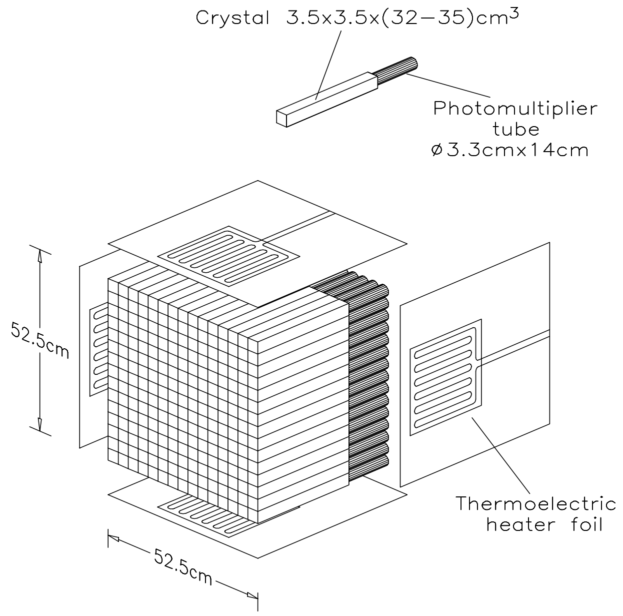

Figure 3.3: High resolution calorimeter module consisting of 15 $\times$ 15 array of crystals, support structure and temperature control.

structure of the Pb/scintillator calorimeter. With the present calorimeter design, one vertical column of Pb/scintillator supermodules can be removed and replaced with corresponding modules of crystals. The adjacent columns of Pb/scintillator supermodules can then be pushed together to form a complete wall, as shown in Figure 3.3. In doing so, some of the outermost Pb/scintillator modules, which are presently uninstrumented, could be equipped with the phototubes and electronics from the modules which were removed from the center of the wall, resulting in no loss in acceptance.

The crystals will be packaged in modules of 15 $\times$ 15 crystals placed inside a thin-walled stainless steel container held together under slight compression as shown in Figure 3.3. The container will have attachments on the back for supporting or removing the modules after they are placed inside the calorimeter. The crystals, including their packaging, will form a close packed array with minimal gaps and dead material in between, as required in order to maintain good energy resolution. Each module will have its own temperature control system using thin foil heaters to maintain the temperature to approximately $30 \pm 1°$C. The temperature will be monitored to better than 0.1°C. Temperature variations should, however, be minimized by the large thermal mass provided by the surrounding Pb/scintillator calorimeter.

The high resolution detector will utilize the existing readout electronics, including ADC's, TDC's and cables, from the Pb/scintillator modules it replaces. However, because of the increased granularity, it will require approximately 2000 additional channels of electronics and cables to fully instrument the detector. The high resolution detector will use a separate high voltage system which will provide a higher degree of stability and greater immunity to noise.

Chapter 4

Techniques and Performance

In this chapter we review the relevant techniques for a precision prompt photon measurement and confront the general requirements with the main features of the proposed detector. The general strategy to measure prompt photons is discussed in some detail in [39]. In addition, we have taken into account recent experience gained by active experiments [40, 5, 14, 41]. We will concentrate in particular on the challenges related to the detection of fairly low $p_t(\leq 3.0$ GeV/c) photons. These photons most likely will contain information about the phase of the matter created in the collision. As discussed in Chapter 3 the quality of the photon measurement will depend much on the S/B ratio for π^0 meson detection. Our proposed detector is positioned at $\theta = 90°$, implying $E_\gamma \approx p_t$. In addition, the multiplicity of hits in the detector increases strongly towards lower energies. Consequently, the low energy performance of the detector in a high multiplicity background is extremely important. A summary of the main requirements on the proposed detector are:

- Identification and Accurate Reconstruction of Photons
- Accurate Measurement of the Photon Energy and Position

In addition, a prompt photon measurement requires

- Understanding of Statistical and Systematic Uncertainties in Meson Reconstruction
- Understanding of the Effects of the Expected High Multiplicity Environment on Resolution and Reconstruction Efficiency

In the following we will discuss these points in detail, with particular emphasis on realistic performance simulations for the proposed detector. We will conclude this section with a summary of the p_t range accessible with the present detector for π^0 measurements, η measurements, and prompt photon detection.

4.1 Photon Identification

In the proposed high resolution photon detector, photons are identified using information from both the photon detector itself and from other detectors in the experiment. One has to distinguish photons from both charged particles and other neutral particles that deposit energy in the detector. The principle tools for photon identification are:

1. charge and momentum measurement from the PHENIX tracking system,
2. time-of-flight measurement,
3. determination of shower shape.

The overwhelming part of the charged particle background consists of hadrons, mostly $\pi^{\pm}$ mesons. At midrapidity their p_t spectrum is expected to be soft, dominated by a thermal type $dN/dp_t^2 \approx m_t\ \exp(-m_t/T)$ distribution, where m_t is the transverse mass, and $T = T_f \approx 0.15$ GeV is the freeze-out temperature. They will be identified and their momentum measured in the PHENIX tracking system. Even for those charged hadrons not fully tracked there will be a charge identification by the signal in the last pad chamber just before the electromagnetic calorimeter. Photon identification consequently starts with the elimination (or tagging) of all hits due to charged particles.

Furthermore, the axial field in PHENIX provides a momentum cutoff below which charged particles that originate at the interaction vertex curl up in the field and never reach the detector. This cutoff is 50 MeV/c and 110 MeV/c for the two planned field configurations, eliminating 2.7% and 12% of the charged pions, respectively. However, this cutoff applies only for particles originating from the interaction point. There may be a significant low momentum background from particles not produced at the vertex. Both secondary interactions in the experimental apparatus (magnet, other detectors) and decays of short-lived particles contribute to this background.

Time-of-flight measurement is another important tool to identify those charged particles who might not have registered in the tracking system. More importantly, it can be used to separate photons from other neutral particles such as neutrons and antineutrons generated in the collision. Also secondary photons and other neutral background can be eliminated very efficiently. The

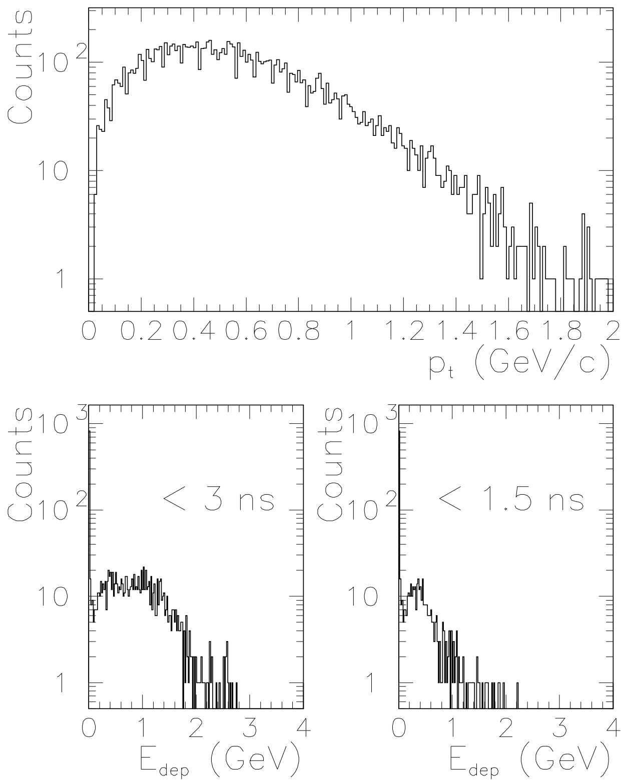

Figure 4.1: Top panel: simulated momentum distribution of antineutrons. Bottom left and right panels: energy deposition of antineutrons that arrive within 3.0 ns and 1.5 ns of a v=c particle.

proposed detector will provide excellent time resolution. Measurements with BaF_2 crystals have produced excellent time resolution in the range of 100 ps for energies larger than 50 MeV [23] [45], independent of energy. In a secondary beam at TRIUMF we tested the time resolution for both BaF_2 CsI crystals of the same dimensions as will be used with the full detector. The time resolution obtained was 55 ps with BaF_2, independent of particle species, and 95 and 125 ps, respectively, for pions and electrons with CsI.

Assuming, conservatively, a time resolution of 250 ps for the full detector and requiring at least 4σ between photons and other particles at 5.1 m distance from the interaction point eliminates all particles with $\beta \leq 0.94$, *i.e.* pions below 0.39 GeV/c and nucleons below 2.6 GeV/c momentum. Using the thermal spectrum described above, this cut rejects 65% of charged pions based on time-of-flight alone, as well as virtually all nucleons (shower overlaps are not taken into account here). Rejecting nucleons is particularly important because of the sizeable background from antineutrons. As pointed out in [46] calculations with current event generators predict a ratio of $\bar{n}/\pi^0 \approx 0.03 - 0.06$ at mid-rapidity. However, in addition to their kinetic energy, antineutrons may deposit up to twice their rest mass in the detector. This leads to a serious background for the prompt photon measurement. In order to study this background quantitatively we have performed detailed Monte Carlo simulations. Typical results are shown in Figure 4.1. Once a 1.5 ns (3.0 ns) cut is applied, only 3.9% (4.6%) of the antineutrons deposit energy within the time window of the prompt photons. From these numbers one can calculate effective "γ"/π^0 ratios using the energy deposit of those antineutrons within the time cut. With a 1.5 ns cut, these effective "γ"/π^0 ratios are well below 1%, even for $\bar{n}/\pi^0 = 0.06$. This should be contrasted with an expected "γ"/π^0 value in excess of 0.5 near $p_t = 1$ GeV/c, which is large as compared to the expected signal, if there is no time-of-flight information at all. Similar simulations indicate that background from neutrons and K_L^0 is not as severe as that from anti-neutrons, and is completely eliminated by the time-of-flight measurement.

A third technique to distinguish photons from other particles, again based solely on information from the photon detector, is to compare the total energy of a shower to the shower size (the number of crystals with energies above an appropriate threshold). We have studied this question extensively both with test beams and Monte Carlo simulations in the 0.05-1.0 GeV energy region. For hadrons the distribution of the number of crystals hit is asymmetric because of the possibility of hadronic interaction in the detector. We have extracted the percentage of pions that are properly distinguished from photons, requiring 90% photon efficiency, if the identification is based *only* on the energy of the shower and the number of crystals hit. Results are shown in Figure 4.2. The cut is quite powerful, even at the lowest momenta: 92-95% of pions are properly identified. The significance of this result is that it provides electron/pion and photon/pion separation already at the trigger level, without relying on momentum information from the tracking devices in front of the detector. This can be used to develop an effective trigger on electromagnetic energy in the proposed detector. The hadron rejection power can be further enhanced offline using the lateral shower dispersion analysis [47].

Once the momenta of charged particles are known from tracking, the mismatch between momentum and deposited energy is an additional valuable tool for charged pion rejection. This was studied with beams of electrons and pions in the test measurements. In Figure 4.2 we also present the measured π/e separation in the 0.1-1.0 GeV/c momentum range, utilizing the comparison of the measured momentum with the energy deposited in the high resolution

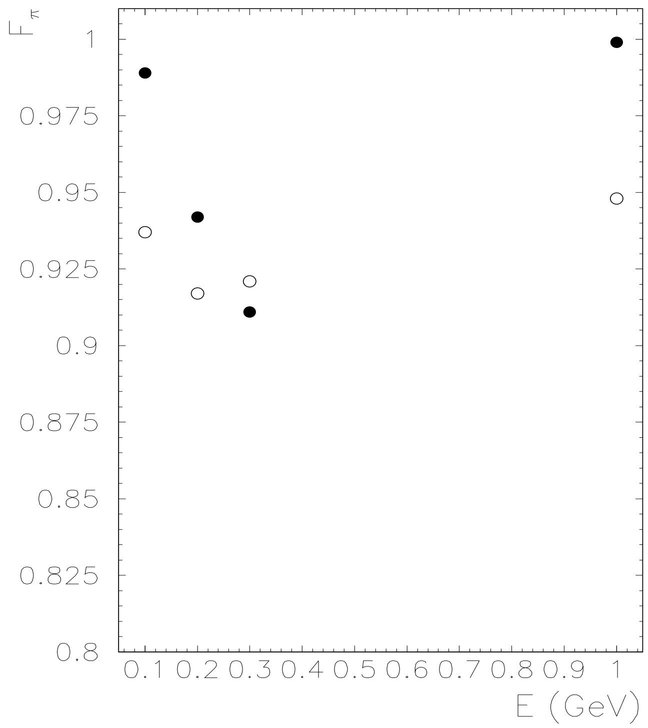

Figure 4.2: Measured pion rejection in the high resolution photon detector. Open symbols: fraction of pions F_π properly distinguished from photons by comparing shower energy with shower size (90% photon efficiency). Solid symbols: fraction of pions properly distinguished from electrons via mismatch of the deposited energy and the momentum ($>$ 95 % electron efficiency).

calorimeter. In addition to the π/e separation, tracking information helps to identify clean photon showers in a high multiplicity environment through an additional isolation cut against charged particles.

In summary, the combination of charged particle tagging and momentum measurement with the PHENIX apparatus and time-of-flight and shower shape measurements in the high resolution detector will provide photon identification with unprecedented quality.

4.2 Measuring Photons with High Precision

In order to measure photons with high precision, the following topics have to be addressed:

1. energy containment (longitudinal size) *vs* light collection uniformity,

2. calibration and gain equalization,

3. monitoring of gain changes,

4. noise,

5. linearity of the detector read-out chain over a wide dynamic range,

6. identification and separation of partially overlapping showers,

7. the effect of material between the collision point and the front face of the photon detector.

We parameterize the energy resolution of the detector in the following way:

$$\sigma/E = \alpha/\sqrt{E(\mathrm{GeV})} \oplus \beta/E(\mathrm{GeV}) \oplus \gamma. \tag{4.1}$$

Our aim is to build a detector with $\alpha \leq 2\%$, $\beta \leq 0.2\%$ and $\gamma \leq 1\%$. Below we will discuss how points 1 to 7 above contribute to the performance of the proposed detector.

1. There are extensive studies in the literature on longitudinal development of electromagnetic showers (see, *e.g.* [48]). The optimal longitudinal size of the crystals is in the range $14 - 20X_0$ where X_0 is the radiation length. At and below 1.0 GeV the parameterization of [48] and GEANT studies result in a longitudinal leakage of about 1.0% (2.5%) at 1 GeV (5 GeV) for a 17 X_0 deep detector. Fluctuations in this leakage contribute to the energy resolution by leading to non-Gaussian low-energy tails. These leakage fluctuations have been studied again with GEANT and using the parameterization of [49] with the result that for crystals at least 16 X_0 deep the fluctuations contribute less than 0.2% (0.6%) to γ for energies less than 1 GeV (5 GeV).

2. Absolute calibration and gain equalization will be done using several independent methods including cosmic rays, π^0 mesons reconstructed from low multiplicity data and identified electrons whose momentum is known from the PHENIX tracking system. The technical implementation is described in Chapter 5. We anticipate that with an effective calibration procedure the contribution to the energy resolution will be below 0.5%.

3. While the light output of the crystals is not expected to change abruptly, both short and long term variations are anticipated in the readout system, especially in the photomultiplier tubes. We are planning to use a pulsed laser gain stabilization system, similar to the one used already in the test setup. The planned system is described in Chapter 5.

4. Based on the test results described in Chapter 5 our aim is to keep the noise in every channel below 1.0 MeV, and the total noise in the sum of 3x3

crystals below 3.5 MeV. This will be the main contribution to the β term in the resolution expression and corresponds to $\beta = 0.35\%$.

5. Nonlinearities in the detector stem mainly from the readout. They lead to systematic errors in the invariant mass reconstruction. In the test setup the maximum nonlinearity is $< 1\%$ for energies from 50 MeV to 6 GeV. The final detector, with lower gain phototubes, should exhibit even lower nonlinearities.

6. We have simulated the performance of the detector in a high multiplicity environment, to study principally the effect of overlap of showers on resolution. Results and analysis strategies are discussed in Chapter 4.4.2. With only 30% loss of efficiency the energy resolution of the proposed detector can be maintained even at particle densities corresponding to three times the multiplicity predicted by the event generator HIJET [56], *i.e.* $dN_{\pi^0}/dy \approx 1000$ (see Table 4.1).

7. The total thickness of material in front of the high resolution detector in PHENIX is approximately 10% of a radiation length. This material between the collision point and the detector causes pair conversion for photons and energy and angular straggling for electrons. After pair conversion the photon can be vetoed if conversion occurs before the last pad chamber and the corresponding particle loss must be corrected for in any quantitative analysis. Since conversion also increases the occupancy in the photon detector, there is a strong incentive to keep the amount of material in front of the detector as low as possible. If photon conversion occurs after the last pad chamber, *i.e.* close to the detector, the consequence would only be a slight broadening of the shower due to the e^+e^- separation. Furthermore this late conversion probability is very low ($< 1\%$).

For electrons, energy loss in the material before the photon detector introduces a low energy, non-Gaussian tail into the detector response. The test results indicate that the energy resolution decreases from a nominal $2\%/\sqrt{\mathrm{E(GeV)}}$ to $2.2\%/\sqrt{\mathrm{E(GeV)}}$ for 200 MeV/c electrons if 0.1 X_0 material is present in front of the detector.

4.3 Distinguishing Direct from Decay Photons

Once photons have been properly identified and their energy measured with high precision, the major difficulty in a direct photon measurement is the distinction between direct photons and photons from meson decays. The general techniques how to separate decay photons from promptly produced photons were developed in the past decade and are described in Chapter 2.1. The major new problems arising for a prompt photon measurement at RHIC at twofold:

1. The expected signal is concentrated at much lower p_t than in hadron-hadron collisions.

2. The overall particle multiplicities are increased dramatically.

Since the p_t spectrum increases strongly as p_t decreases, both points lead to a severe reduction in signal to background ratio S/B for the reconstruction of neutral mesons decaying into two photons ($S/B \propto 1/(dN/dy)$). The need to measure their spectra accurately down to p_t values of 0.3 GeV/c (for π^0 mesons) and 1.4 GeV/c (for η mesons) in the high multiplicity environment of Au+Au collisions at RHIC has led to the design of the proposed detector, with unprecedented requirements on energy resolution, time resolution, and granularity.

In principle, one has to take into account, for the direct photon measurement, any hadron that has a decay branch into photons. However, higher mass hadrons are produced at a much lower rate and/or their branching ratio for electromagnetic decays is small [14]. In the following discussion we will therefore concentrate on the two dominant background sources, *i.e.* π^0 and η mesons.

If the total number of photons N_γ in the detector is low and the acceptance is large as compared to the typical opening angle θ of the meson decay photons, the real decay pairs can be selected with efficiency $\epsilon \approx 1$, and the meson spectra can be measured via directly identified decay photon pairs. The remaining photons are considered to be direct photons and the error introduced is $O(1-\epsilon)$. This is a technique which has been used successfully for the study of photon production in hadron-hadron collisions (see Chapter 2.1). At RHIC multiplicities this technique is applicable for high p_t photons and mesons (> 7 GeV/c for heavy ion interactions) until the merging of showers prevents π^0 reconstruction, *i.e* $p_t > 25$ GeV/c, much beyond the region addressed with this proposal.

If the multiplicity is high, or the acceptance is small, the efficiency to properly identify decay pairs will be very low. In this case meson spectra (usually expressed as dN_π/dp_t) can be measured statistically. Rather than trying to identify event by event those photon pairs originating from meson decay, invariant mass spectra will be generated by pairing for each event every photon with every other photon in the detector. The invariant mass $M_{\gamma\gamma}$ reconstructed from real pairs (two photons from the same meson) will peak

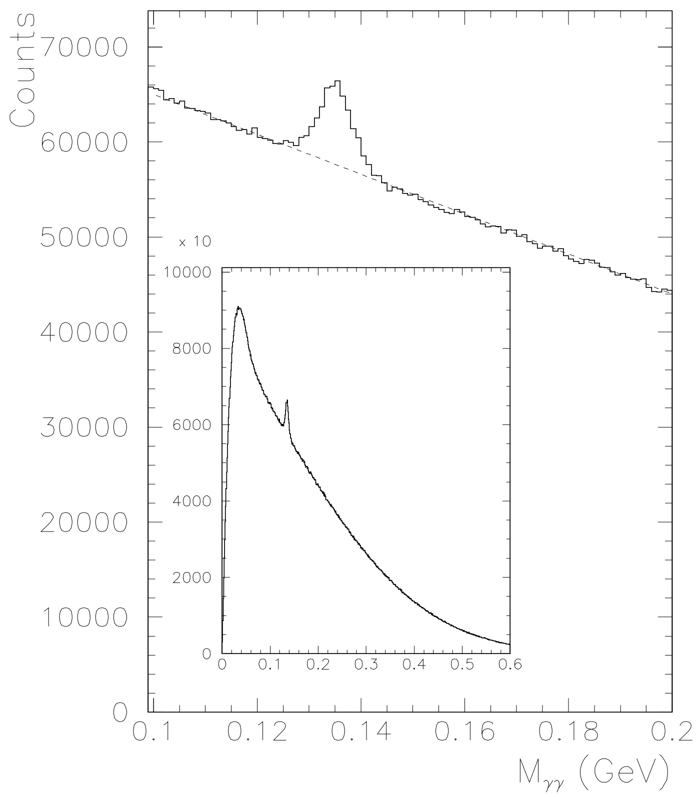

Figure 4.3: Insert: typical invariant mass distribution in the proposed acceptance ; $dN_{\pi^0}/dy = 330$, transverse momentum of the photon pair $0.8 \leq p_t^{\gamma\gamma} \leq 1.0$ GeV/c. The main plot is the region around the π^0 peak with a polynomial fit to the combinatorial background, used to obtain the integral of the peak. See the text for details.

at the meson mass, smeared out according to energy and position resolution of the detector. However, this signal S will be superimposed on a very large combinatorial background B $\propto (dN/dy)^2$ of all accidental combinations with the same invariant mass, leading to $S/B \propto 1/(dN/dy)$ as quantitatively discussed in Chapter 3. The S/B ratio can be enhanced by a cut on the energy asymmetry a defined as $a = (\mid E_{\gamma_1} - E_{\gamma_2} \mid)/(E_{\gamma_1} + E_{\gamma_2})$.

A typical invariant mass distribution expected with the proposed detector is shown in Figure 4.3. Note the clear π^0 peak and the relatively large S/B ratio for the π^0 reconstruction, despite the high multiplicity and relatively low transverse momentum. The main reason for this is the excellent energy resolution of the proposed detector.

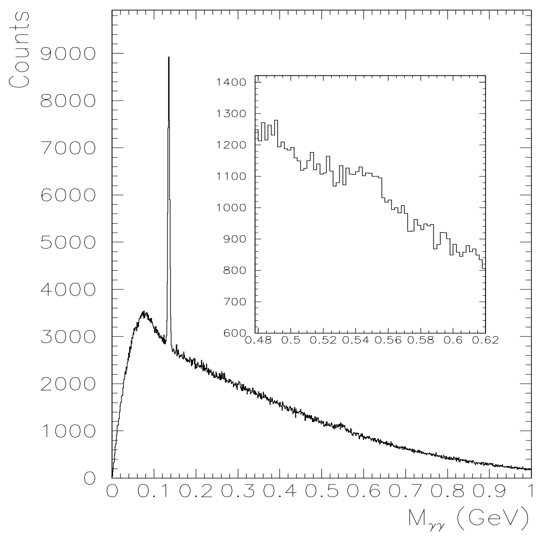

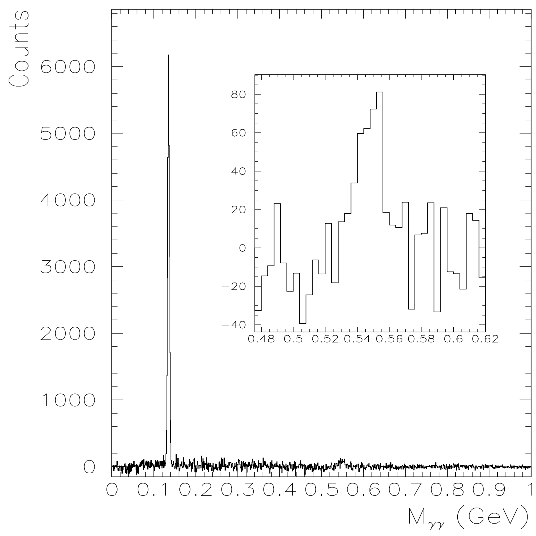

Figure 4.4: Invariant mass distribution of photon pairs with $p_t > 1.4$ GeV/c with an asymmetry cut $a < 0.2$. Top: the original invariant mass distribution with the η region enlarged (insert). Bottom: invariant mass distribution after mixed event subtraction and again, the η region enlarged (insert).

Even more stringent requirements are placed on the detector for the reconstruction of η mesons from their two photon decay. First the efficiency for η meson detection is significantly lower than that for π^0 mesons because for a given p_t the opening angle between the decay photons is increased by the ratio of the masses $m_\eta/m_\pi \approx 4$. Secondly, the S/B ratio is small for the η meson because S is reduced by the η/π ratio and the 39% branching ratio for η decay into two photons, and B contains combinatorial background from both η and π mesons. Nevertheless, with the proposed detector one can reconstruct η-mesons for $p_t \geq 1.4$ GeV/c, as is indicated in Figure 4.4. For this calculation we have assumed that the η/π^0 is fixed at 0.55, rather than using m_t scaling as elsewhere in the Monte Carlo simulations. At $p_t \geq 1.4$ GeV/c this enhances the η peak by about a factor of 1.8 and was done to get statistics in the Monte Carlo calculation. The statistics underlying Figure 4.4 is based on $1 \cdot 10^7$ central collisions corresponding to about three days of Au+Au running at RHIC. As is obvious from Figure 4.4, the η peak is quite visible, even before subtraction of the combinatorial background, when one reconstructs those $\gamma\gamma$ pairs with $p_t^{\gamma\gamma} \geq 1.4$ GeV/c. Here, $p_t^{\gamma\gamma}$ is the magnitude of the vectorsum of the transverse momenta of the two photons. With sophisticated background subtraction techniques (mixed event method, see below) the peak stands out quite prominently, as shown in Figure 4.4.

The signal S, *i.e.* the true number of reconstructed π^0 mesons, is the integral of the peak above the combinatorial background. Equivalent to the S/B ratio one can characterize the performance of the detector in terms of the peak/total ratio $Q = S/(B+S)$, the integral of the peak itself divided by the integral of the entire region around the meson mass. Obviously this ratio Q depends on the p_t region considered and increases with increasing p_t. Furthermore, Q scales inversely with the energy resolution (actually the invariant mass resolution, determined by energy and angular resolution, see eq. 3.1) of the detector since B depends on the width of the meson mass peak. As long as errors are dominated by counting statistics (Q is in the few percent range or above) the relative error of the extracted π^0 yield is

$$\frac{\delta N_{\pi^0}(p_t)}{N_{\pi^0}(p_t)} = \sqrt{\frac{2 - Q_{\pi^0}(p_t)}{Q_{\pi^0}(p_t) N_{\pi^0}(p_t)}} \tag{4.2}$$

There are two basic methods to determine the integral of the the peak itself, or equivalently, to estimate the combinatorial background under the peak. In the first method, the invariant mass is generated only from photon pairs of the same event ($M_{\gamma\gamma}^{real}$). The combinatorial background is obtained by fitting a (polynomial) function to the distribution of the invariant mass $M_{\gamma\gamma}$ below

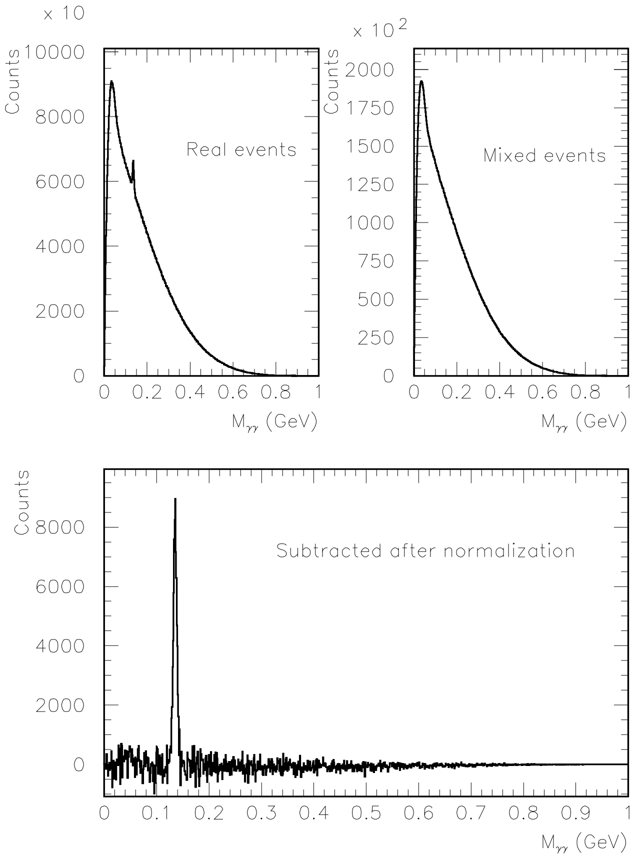

Figure 4.5: Illustration of the event mixing technique. Top left: distribution of the invariant mass $M_{\gamma\gamma}^{real}$ ($dN_{\pi^0}/dy = 330$, $0.8 < p_t < 1.0$ GeV/c). Top right: invariant mass spectrum from mixed events. Bottom: difference between top left and top right, normalized such that the integral from 0.06 to 0.11 GeV is zero.

and above the meson mass. An example of this is illustrated in Figure 4.3.

In the other technique, pioneered by the WA80 Collaboration [14] the combinatorial background is determined with very high statistical precision by event mixing. This requires two invariant mass distributions to be generated. The first uses the same $M_{\gamma\gamma}^{real}$ as above, consisting of combinations of all photons in the same event. For the second distribution all photons from one event are paired with all photons from a different event of the same event class, and the resulting $M_{\gamma\gamma}^{mix}$ distribution is considered to be the combinatorial background. After proper normalization the distribution of $M_{\gamma\gamma}^{mix}$ is subtracted from the distribution of $M_{\gamma\gamma}^{real}$. The integral of the remaining peak is the number of π^0 mesons. The procedure is illustrated in Figure 4.5. Now the π^0 signal stands out dominantly from the remaining background.

For the proposed experiment it is extremely important to understand both the statistical and systematic accuracies in the signal determination. It has been shown recently [53] that both methods (function fit and event mixing) introduce systematic errors in the number of extracted pions. For high statistics samples the errors are usually in the few percent range, not negligible for a precision measurement. However, this error can be corrected with an iterative Monte Carlo procedure. Nevertheless, in a precision measurement it is important for the understanding of possible systematic errors to be able to use the direct (function fit) yield extraction at all p_t values relevant for the experiment, in addition to the mixed event technique, providing an independent cross-check of the yields.

From the reconstructed meson signals S one can determine the meson transverse momentum spectra. The proposed detector, and indeed, the whole PHENIX central detector, cover only a fairly small (pseudo)-rapidity range centered about midrapidity. Mesons with rapidities outside this acceptance can emit photons which hit the high resolution detector. To take this into account one has to extrapolate the meson invariant cross sections over a rapidity range of $\approx \pm 1$ unit. We will show below that the uncertainty in this extrapolation does not introduce a large uncertainty into the prompt photon measurement.

Once the meson yields are known as a function of y and p_t, it is straightforward to calculate, by Monte Carlo methods, the expected number of decay photons in the detector. All mesons that make a significant contribution to the number of photons in the detector have to be included although the dominant sources are π^0 and η decays [14, 23]. Any excess photons are then considered to be direct photons. Considering background from π^0 and η decays only the number of direct photons N_γ^{dir}, or equivalently, the γ/π^0 ratio at a given p_t, is given by for π^0 and η

$$\frac{\gamma}{\pi^0} = \frac{\varepsilon_{\pi^0}}{\varepsilon_\gamma}\left(\frac{N_\gamma^{obs}}{N_{\pi^0}^{obs}} - \frac{N_\gamma^{\pi^0}}{N_{\pi^0}^{obs}} - \frac{N_\gamma^{\eta}}{N_\eta^{obs}}\frac{N_\eta^{obs}}{N_{\pi^0}^{obs}}\right) \tag{4.3}$$

Here $\varepsilon_{\pi^0}, \varepsilon_\gamma$ are the photon and pion detection and reconstruction efficiencies, $N_\gamma^{obs}, N_{\pi^0}^{obs}, N_\eta^{obs}$ are the numbers of observed photons, π^0 and η mesons. Further, $N_\gamma^{\pi^0} and N_\gamma^{\eta}$ are the numbers of photons into the detector acceptance from the decay of the corresponding meson, computed from the measured and extrapolated meson distributions. The equation can be generalized in a straightforward way for higher mass mesons if necessary. As pointed out earlier (see Chapter 2.1) the direct photon signal from the QGP expressed as γ/π^0 can be as low as few percent if the initial temperature is low. The error on the π^0 yield itself will limit the sensitivity of the direct photon measurement. We have considered the following four sources of errors:

- The statistical and systematic errors in extracting the number of mesons S from the invariant mass distribution.
- The discretization of the meson p_t spectrum (because the yields are extracted in finite p_t bins and then interpolated in order to reconstruct the original continuous distribution).
- The limited rapidity coverage (pions away from $y = 0$ will produce photons into the detector acceptance, particularly at low p_t).
- The uncertainty in the geometrical and reconstruction efficiency ε as a function of multiplicity

The cumulated effect of the yield extraction error and spectrum discretization is illustrated in Figure 4.6, where the ratio of two transverse momentum distributions is plotted. The input distribution is generated using a thermal meson p_t spectrum, with $dN_{\pi^0}/dy = 300$, constant over ± 2 units of rapidity around $y = 0$. The energies and positions of the decay photons are folded with the detector resolution resolution before the invariant mass of photon pairs is calculated. From the invariant mass spectra the transverse momentum distribution is calculated and plotted in p_t bins of 200 MeV/c width. The total number of events is $2 \cdot 10^6$ (corresponding to about 12 hours running time with 50 central collisions/s). This p_t distribution is extracted from the photon spectra with the same procedure that will be applied in the actual data analysis. It contains the statistical and systematic errors due to acceptance, yield extraction and p_t binning. Obviously the ratio of the original and reconstructed distributions should be unity. The actual deviations are within 1.5%, indicating that these uncertainties will not be the limiting factors in the measurement.

Limited rapidity coverage introduces another uncertainty. Currently we assume a rapidity plateau over ± 2 units of rapidity around $y = 0$. The EM calorimeter in PHENIX will measure dN_{π^0}/dy in the range $-0.35 < y < 0.35$. Beyond these limits we will use the Si-vertex detectors of the PHENIX experiment to determine, for the sample of events under consideration, the pseudorapidity distributions of charged particles. In Figure 4.7 we show that in this scenario the fraction of the decay photons in the detector coming from mesons with rapidity $\mid y \mid \geq 0.35$ and $\mid y \mid \geq 1.5$ is quite small. This fraction in the range $\mid y \mid \geq 0.35$ is for instance 0.055 for photons in the range $0.6 < p_t^\gamma < 0.8$ GeV/c. Assuming that we know the distribution to within 10% from the

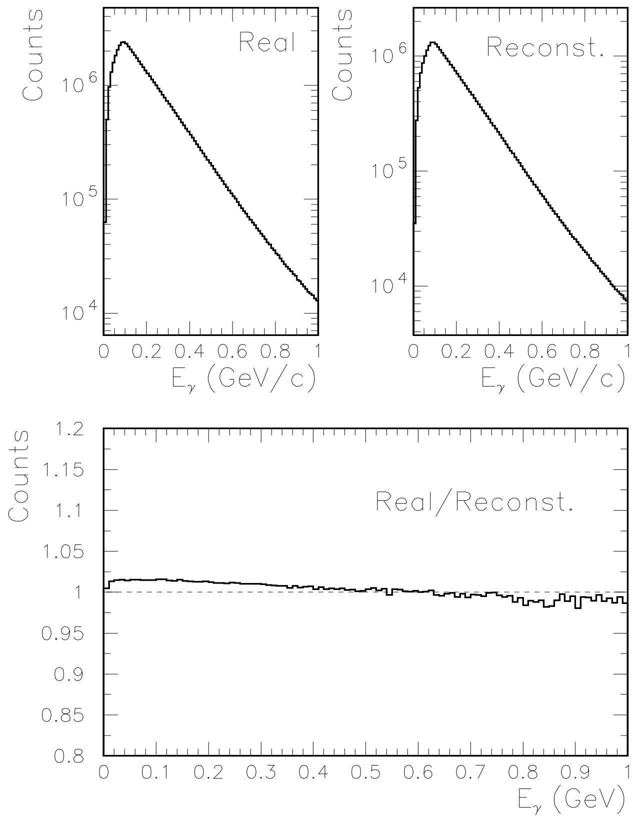

Figure 4.6: Errors in the decay photon yield reconstruction. Top left: decay photon spectrum from an assumed (perfectly known) thermal meson spectrum (π and η). Top right: decay photon spectrum from the reconstructed (measured) meson spectrum. Bottom: ratio of the original and the reconstructed decay photon spectra. See text for details.

other PHENIX detectors introduces a systematic error of $0.055 \cdot 10\% = 0.55\%$ into the extraction of direct photons. This estimate is pessimistic as it uses a flat rapidity distribution. Currently all event generators predict a Gaussian rapidity distribution for pions. For the case of HIJET [56], *e.g.*, the prediction for dN_π/dy is a Gaussian centered at $y = 0$ with a standard deviation of $\sigma = 2.6$.

4.4 Monte Carlo Simulations

For most of the simulations discussed in this section we used a π^0 p_t distribution (see Figure 4.8) as given in eq. 2.4. Further, η mesons were generated using

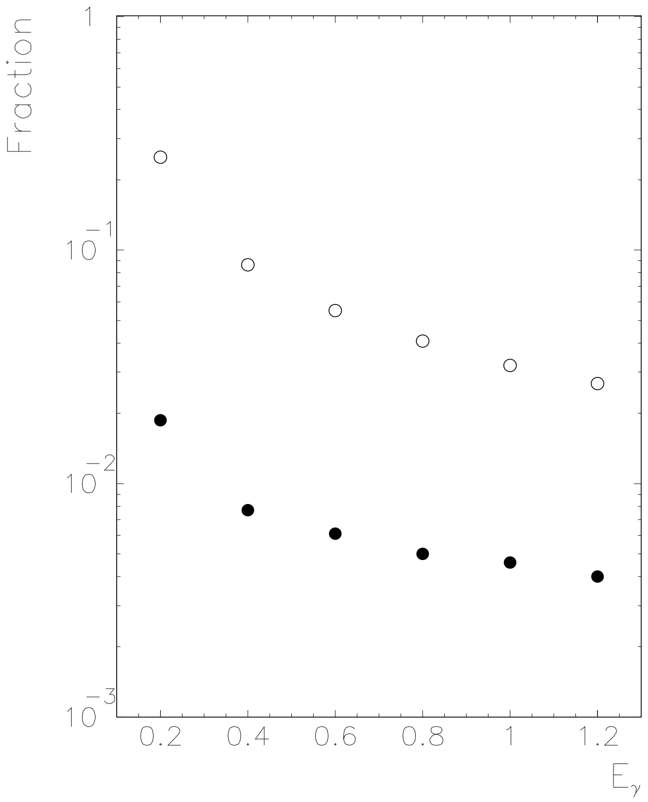

Figure 4.7: Effects of limited rapidity coverage: fraction of photons with a certain p_t in the high resolution detector that originate from π^0 mesons with rapidity $\mid y \mid \geq 0.35$ (open circles) and $\mid y \mid \geq 1.5$ (closed circles) assuming $dN/dy = const$ for the mesons at $\mid y \mid \geq 2.0$.

m_t scaling, with an asymptotic ratio $\eta/\pi^0 = 0.55$ and let decay into two photons with 38.9% branching ratio. The $\eta \rightarrow 3\pi$ modes were considered to be part of the π^0 spectrum. We assumed either a constant rapidity density $dN_{\pi^0}/dy = 330$ or a Gaussian with $\sigma = 2.6$, a peak of 330 and centered at $y = 0$, close to the prediction of the event generator HIJET [56]. To check the performance for very high multiplicities we also calculated the response of the detector to double and triple HIJET events.

To make conservative estimates we assumed an energy resolution of the detector of $2\%/\sqrt{\mathrm{E(GeV)}}$. The position resolution was taken into account as an angular uncertainty of $0.1°$. Note that the actual position resolution should lead to a better angular resolution for all but the lowest photon energies $\mathrm{E}_\gamma <$ 0.2 GeV.

The kinematic acceptance of the detector is shown in Figure 3.1 where the

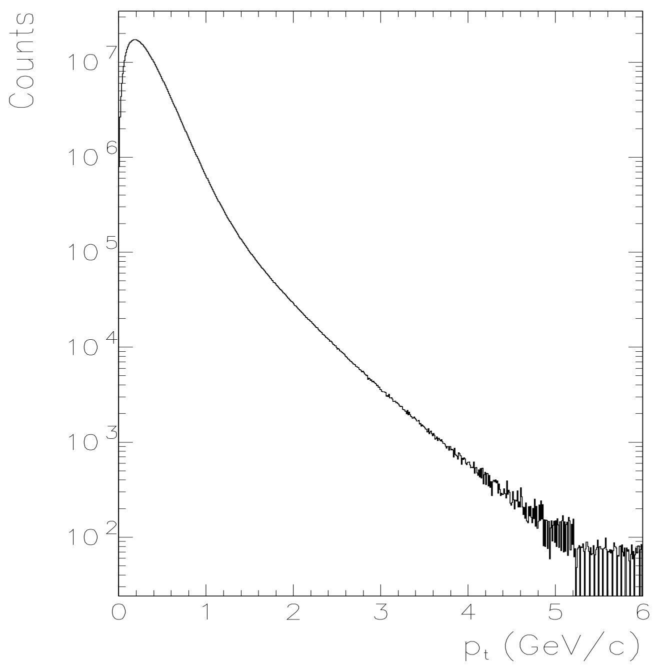

Figure 4.8: Transverse momentum distributions for π^0 (and η) mesons used for the simulations of detector performance.

number of accepted photon pairs per 10^7 events is plotted for both π^0 and η mesons as a function of the transverse momentum.

4.4.1 Peak/total Ratios for π^0 and η Mesons

The measurement of direct photons depends on the precise measurement of the yield of mesons that have photon decay channels. As discussed above and in Chapter 3, the signal-to-background ratio S/B or, equivalently (for $S << B$) $Q = S/(B+S)$ for the two-photon invariant mass distributions depends strongly on the multiplicity density dN/dy. In order to check the simple analytic prescription given in Chapter 3 and to perform a systematic study of this dependence, we have calculated Q for π^0 and η meson reconstruction in the proposed detector as function of p_t for different multiplicity densities.

The invariant mass was calculated as a function of the transverse momentum of the photon pair $p_t^{\gamma\gamma}$ in 0.2 GeV/c bins. The background above and below the meson peak (outside $\pm 2\sigma$) was fitted with a polynomial. When extracting the peak/total ratios both the peak and the fitted background were integrated in the $\pm 1\sigma$ range. The procedure was repeated by applying an

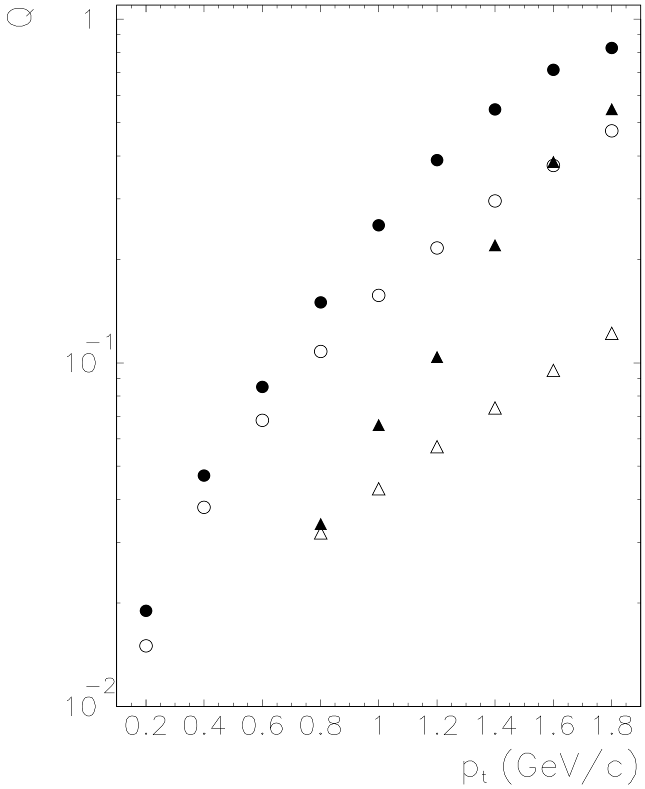

Figure 4.9: Peak/total ratios Q in the 2γ invariant mass plot for π^0 mesons as a function of $p_t^{\gamma\gamma}$ for colliding beams of 100 GeV/nucleon. The rapidity density is $dN_{\pi^0}/dy = 330$. Circles: the proposed high resolution detector. Triangles: the PHENIX electromagnetic calorimeter. Open symbols: all pairs. Solid symbols: an asymmetry cut $a \leq 0.2$ is applied.

$a < 0.2$ cut on energy asymmetry of the two photons. Results are shown in Figure 4.9 and Figure 4.10 for π^0 and η mesons, respectively. Even for $p_t^{\gamma\gamma} = 0.5$ GeV/c Q is 8%. The results are in good agreement with the simple prescription given in Chapter 3, which then can be used to extrapolate to other rapidity densities.

4.4.2 Resolution and Efficiency in a High Multiplicity Environment

In a high multiplicty environment as expected for Au+Au collisions at RHIC, it is important to understand how nearby showers can affect the occupancy and energy resolution of the high resolution detector. To study this aspect the pixel occupancy was computed under the assumptions that each of the three pion

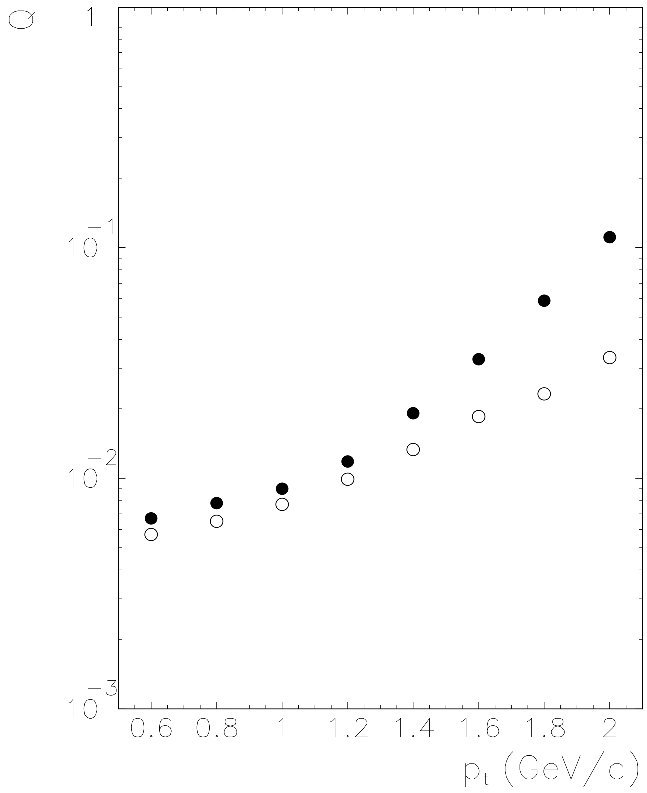

Figure 4.10: Same as Figure 4.9 but for η mesons.

species have a rapidity density $dN/dy = 330$, giving a total rapidity density, including photons from π° decays, of $dN/dy = 1320$. Under these conditions the mean number of particles in the high resolution detector described above is 16.3 photons and 16.3 charged particles (mostly pions). Note that decay in flight of charged pions was not taken into account. Since the decay muons are always minimum ionizing, the shower overlap will be reduced when decays are taken into account. The shower or cluster size is defined as the number of crystals with greater than 1.5 MeV of deposited energy and depends on particle type and energy. With this threshold, an energy resolution of $2\%/\sqrt{E(\mathrm{GeV})} \oplus 1\%$ can be maintained even at the lowest energies. Using thermal pion spectra and folding hits in the detector with the appropriate shower sizes, the pixel occupancy is only 3.9%.

If the distance between the centers of gravity of overlapping showers is greater than approximately 2 R_M, the showers can be decomposed but the overlap will result in some deterioration of the energy resolution of each shower. However, if they are closer together, it may not be possible to determine

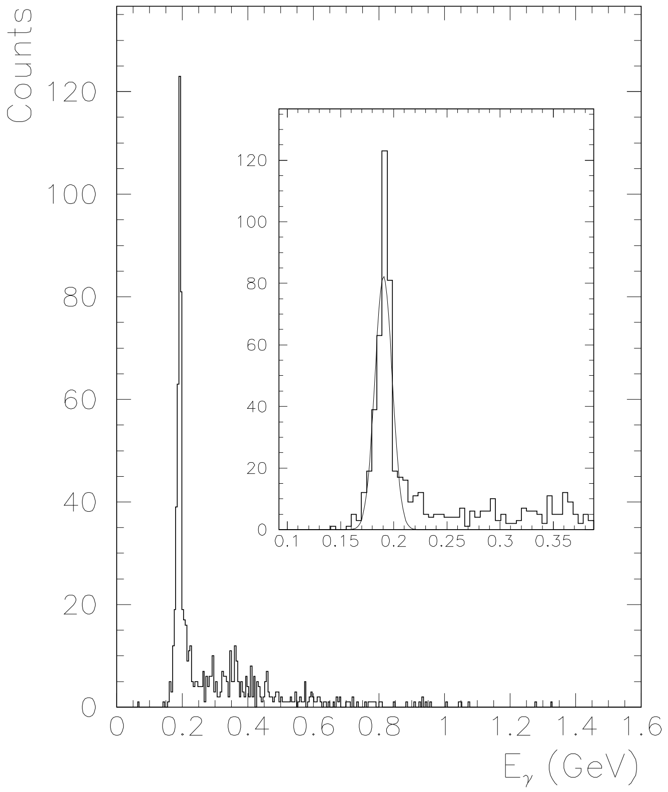

Figure 4.11: Measured energy of 200 MeV photons within double HIJET events ($dN_c/dy = 1500$).

the energy of either shower with the required precision. In this case, both showers will be rejected, leading to a loss in efficiency. In fact, for shower separations of less than $\approx 1\ R_M$, two showers might be misidentified as one. However, because of the low occupancy in the high resolution photon detector, the probability to get any two showers in an event within $1\ R_M$ is less than 4%, even for triple HIJET multiplicities.

The photon reconstruction efficiency enters directly into the determination of the γ/π^0 ratio because the reconstruction of π^0 and η mesons requires simultaneous reconstruction of a pair. The trade-off between efficiency and resolution therefore needs to be quantitatively understood in any direct photon analysis. Measurements and studies of the WA80 and WA98 collaborations [14, 41] imply that for multiplicity densities equivalent to triple HIJET multiplicities the occupancy in the proposed detector leads to a reconstruction efficiency of larger than 70% with an uncertainty of less than 3%.

Fig 4.11) shows the simulated effect of high occupancy (double HIJET) on

Table 4.1: Simulated performance of the high resolution photon detector in a high multiplicity environment. The numbers given in the table are the absolute photon energy resolution and, in parenthesis, the fraction of photons surviving an energy dependent isolation cut in the clustering algorithm.

E_γ (MeV)	Isolated photon	Single HIJET $dN_c/dy = 740$	Double HIJET $dN_c/dy = 1500$	Triple HIJET $dN_c/dy = 2250$
200	6.7(100%)	7.0(85%)	8.3(70%)	10.1(54%)
500	10.5(100%)	10.8(91%)	11.8(82%)	15.2(75%)
1000	15.0(100%)	21.1(91%)	22.2(80%)	30.1(70%)

the resolution of a 200 MeV photon. The high energy tail visible in the figure can be eliminated with an isolation cut in the cluster algorithm resulting in an 18% efficiency loss. A summary of the expected performance as a function of multiplicity is given in Table 4.1. There, results are presented for 200 MeV, 500 MeV and 1 GeV photons in events with multiplicities corresponding to single, double and triple HIJET. The absolute widths of the photon peak are listed in MeV. Because of the importance to keep the efficiency high we have, in this simulation, tried to optimize the reconstruction efficiency even at some loss of resolution. Nevertheless, the results show that even with multiplicities substantially higher than single HIJET, neither the photon resolution nor the photon efficiency deteriorate significantly.

With real data the reconstruction efficiency can be determined by several methods, including mixing single photons of known energy (by Monte Carlo procedures) into real high multipicity events and reconstructing it. Other methods employ superposition of several low multiplicity events. These methods should lead to very accurate determination of the multiplicity dependence of the reconstruction efficiency and we estimate a relative error of less than 3% for the highest multiplicities.

4.5 Summary of Statistical and Systematic Errors

Here we summarize the uncertainties for the determination of the γ/π^0 ratio taking into account all error sources discussed above. Note that the photon reconstruction efficiency enters linearly into this ratio. Therefore:

$$\delta\frac{\gamma}{\pi^0} = \sqrt{(\frac{\delta\pi^0}{\pi^0})^2 + (\frac{\delta\eta}{\eta})^2(\frac{\eta}{\pi^0})^2 \cdot \kappa^2 + (\frac{\delta\varepsilon}{\varepsilon})^2} \tag{4.4}$$

In Table 4.2 we summarize the expected systematic errors for π^0 reconstruction and their estimated size. Due to the high event rates for the high resolution photon detector statistical errors will be small. The situation is somewhat different for η reconstruction. However, the absolute error in γ/π^0 due to the statistical uncertainty in the η/π^0 ratio is $\delta(\gamma/\pi^0) = \kappa(\eta/\pi^0)\delta(\eta/\pi^0)$, where κ=0.39 is the branching ratio for $\eta \rightarrow \gamma\gamma$. If we assume (unrealistically and pessimistically) that $\eta/\pi^0 = 0.55$, independent of p_t, then a 10% uncertainty in the η/π^0 ratio will lead to an absolute uncertainty in γ/π^0 of about 2%.

The running time necessary to get 1% and 10% statistical accuracy for the π^0 and η measurement depends on the signal to total ratio Q. Using Q from our Monte Carlo simulations, the kinematic acceptance of the detector, the expression for the relative error of the measured yield and a RHIC luminosity of $2 \cdot 10^{26}/(\text{cm}^2\text{s})$ one can estimate the running time necessary to extract the meson yield with a given precision. To determine γ/π^0 with a 2.2% statistical accuracy one needs to measure π^0 and η mesons with a 1 and 10% accuracy. The peak/total ratio Q is about 3% for π^0 reconstruction at 0.3 GeV/c and 1% for η reconstruction at 1.4 GeV/c. Therefore, to extract the yields with 1% (10%) error $7 \cdot 10^5$ $(2 \cdot 10^4)$ mesons have to be detected. Folding in the kinematic acceptance (as shown in Figure 3.1) $1.5 \cdot 10^7$ events ($\approx$ 100 hours) are needed to measure the π^0 yield at $p_t = 0.3$ GeV/c with 1% precision and 9×10^7 events ($\approx$ 550 hours) are needed to measure the η yield at $p_t = 1.4$ GeV/c with 10% precision. While this time is not insignificant, it is still short enough for systematic and programmatic studies of the dependence of the photon yield on centrality, system size, *etc.*

In summary, with the proposed detector we will be able to reliably reconstruct π^0 mesons for $p_t \geq 0.3$ GeV/c and η mesons for $p_t \geq 1.4$ GeV/c. Taking the systematic errors in the photon and π^0 measurement into account, we estimate that the γ/π^0 ratio can be measured at $p_t = 0.6$ GeV/c and above if this ratio is larger than 4%. Clearly the dominant source of systematic errors is due to the photon reconstruction efficiency and all efforts need to be undertaken to control this quantity experimentally. The reconstruction efficiency directly improves with better detector resolution and granularity. This consideration was a major driving force for the design of the proposed high resolution, high granularity detector.

Table 4.2: Anticipated sources of systematic errors in the direct photon measurement, the relevant p_t ranges, and an upper estimate on their magnitude

Error source	Dominant at p_t	Size
Calibration		1.0%
Photon reconstruction		<3.0%
Meson yield extraction	0.2 - 1.0 GeV/c	1.5%
Mesons other than π^o and eta		0.5%
Finite η coverage	0.2 - 1.0 GeV/c	0.6%
Quadratic sum		3.6%

4.6 Inclusive Photon Measurement

Measuring direct photon production in the kinematic region below the turnover from the π^0 decay ($p_t < 100$ MeV/c) range is possible without reconstruction of the π^0 mass if other possible sources of background are kept low. These could arise from soft photons generated by hadronic showers produced by other particles in the collision interacting in the material surrounding the detector. As discussed above, most of this background can be eliminated since our planned photon detector has very good time resolution, so that the background photons can be distinguished from those produced inside the interaction region by time-of-flight.

In the p_t range of about 50 to 600 MeV/c, not covered by the direct method discussed above, it is possible to measure the inclusive photon spectrum and compare it with the expected number of photons from hadron decays. Any excess would again signal direct production. Determining this excess requires a precise knowledge of the spectrum of π^0 and other mesons which can produce photons in this p_t range. This can be obtained using the information from the photon detector at higher p_t, as well as from the rest of the PHENIX EM calorimeter. With a detailed knowledge of the spectrum at higher p_t (> 300 MeV/c), one can extrapolate the measurement down to lower p_t and compare it with the observed spectrum. The level of sensitivity for detecting a direct photon signal will depend on the statistical and systematic error of this extrapolation. The considerations above imply that any excess in the few percent range should be observable with the proposed detector.

It is also possible to use the inclusive photon spectrum measured at higher p_t in other parts of the detector to determine the p_t and rapidity spectrum of π^0's and other mesons. This method is originally due to Sternheimer [54] and was further developed by others [55]. It utilizes the technique for deconvoluting the meson decay spectrum from the inclusive photon spectrum measured over various regions of phase space, and has been successfully used by several experiments to measure the inclusive spectrum of soft photons down to extremely low p_t ($\sim$ few MeV/c), even in very high energy hadron collisions [23][28]. In the case of PHENIX, these spectra would be measured using all of the information from the EM calorimeter and used to determine the spectrum for those π^0 mesons which, via their decay, could potentially put a photon into the high resolution detector.

If an excess of direct photons is observed in either the low or intermediate p_t range, it is possible to obtain additional information about their origin by measuring the associated charged hadron multiplicity which accompany the photons. If the photons originate from soft q-$\bar{q}$ annihilation, these interactions will scale as the product of the quark and anti-quark densities inside the hadronic matter. Assuming these are equal in a fireball-like collision, then the number of directly produced photons will vary as square of the quark density, and hence the square of the hadron multiplicity. On the other hand, if the photons are produced by external bremsstrahlung as discussed in Chapter 2, their number will vary linearly with the hadron multiplicity. Hence, correlating any observed signal with the total hadron multiplicity measured in the rest of the PHENIX spectrometer will provide information on the origin of the source of these photons.

4.7 Low Mass Dilepton Pairs *vs* Prompt Photons

As already mentioned above, measurement of the dilepton continuum is sensitive to the thermalization of quarks during the initial state of the collision. In contrast, prompt photon production rates are strongly influenced by the (much earlier) thermalization of gluons [18]. The relative rates for virtual and real photons, respectively, are therefore proportional to n_q/n_g, the ratio of thermalized quarks and gluons, which is much less than 1 in the early stages of the reaction. The two measurements are therefore quite complementary. There are also different backgrounds and experimental problems associated with the dilepton continuum measurement. Here we briefly discuss and compare the signals and backgrounds for both continuum dilepton and prompt photon measurements.

The signal and background for the continuum dielectron measurement has been extensively studied by the PHENIX collaboration [1]. For the comparison with photons one should first mention that the signal for photon production is stronger than that for dilepton production by more than two orders of magnitude (see Chapter 2). The dominant background to the photon measurement is due to π^0 decay, the corresponding background for the di-electron measurement is Dalitz decay of the π^0. In addition to Dalitz decays Drell-Yan dileptons and open charm combinatoric background might dominate the lepton continuum spectrum unless the initial (quark) temperature is very high. We have discussed above how well π^0 decay photons can be measured. Within the PHENIX baseline detector Dalitz rejection can only be performed upon those electron pairs for which both decay particles are detected in the PHENIX acceptance, leading to rejection factors of less than 1.5 in the mass range $0.6 < m_{ee} < 2$ GeV/c^2 (see Fig. 3.4 in ref. [1]). For $dN_\pi^0/dy = 400$ and T$_i$ = 0.25 GeV this leads to a signal/combinatoric background ratio of about 1% for pair masses larger than 1 GeV/c^2 [42], *i.e.* about a factor of 20 below the experimental limit. For the same conditions the expected γ/π^0 is about 6%, certainly measurable with the proposed detector. As discussed in Chapter 3 of [1], measurement of the electron pair continuum from the QGP in PHENIX will most likely have to await the development of an effective inner Dalitz rejection detector.

Chapter 5

Detector Technology and Test Results

5.1 Technology Choices

The high resolution detector must be capable of providing excellent energy, time and position resolution, along with a good signal to noise ratio and low energy threshold for measuring low energy photons. We have considered two techniques for achieving these goals, the first utilizing fast scintillating crystals, and the second utilizing high density cryogenic liquids. We feel that scintillating crystals offer the best solution within the present design of the PHENIX experiment for a number of reasons.

- Crystals have been shown to provide excellent energy resolution in large detector systems with readily available readout technologies and have been operated successfully over extended periods of time in a number of experiments [43][44][45].

- Cryogenic liquids read out in ionization mode cannot provide the required time resolution needed for precise time of flight measurement. High speed crystals, on the other hand, provide excellent time resolution.

- In an optical readout mode, cryogenic liquids offer no advantage over crystals and impose the additional complication of requiring a cryostat. The cryostat is a significant disadvantage for measuring low energy photons because of the increased dead material in front of the active detector, and because of dead material around the sides of the detector which causes gaps in either rapidity or ϕ coverage.

- Even high density cryogenic liquids such as liquid xenon and liquid krypton provide less shower containment than high density crystals. Their larger Molière radius would lead to higher occupancy per unit cell for a given segmentation at the location of our proposed detector.

- Since the rest of the PHENIX EM calorimeter is based on Pb/scintillator and Pb glass with photomultiplier tube readout, scintillating crystals can be integrated into PHENIX calorimeter system in a natural way, utilizing similar methods of support, readout and calibration.

- Substantial production capacitity exists worldwide for producing several types of scintillating crystals which would meet our needs in large quantities and at low cost.

Two different types of scintillating crystals are presently being considered, one being undoped cesium iodide (CsI), and the other barium fluoride (BaF_2). Undoped CsI is a relatively new scintillating crystal with a radiation length of 1.85 cm, a Molière radius approximately 3.8 cm, and fast component light emissions at 310 nm with decay times of 10 ns (67%) and 36 ns (23%), and a slow component (10%) at about 400-500 nm with a decay time on the order of a microsecond. Barium fluoride has a radiation length of 2.05 cm, a Molière radius of approximately 3.4 cm, and light emissions at 220 nm (20%) and 320 nm (80%), with decay times of less than 1 ns and 620 ns, respectively. Both crystals have very high light output, capable of producing several hundred photoelectrons per MeV of deposited energy. We chose, however, to utilize them in a readout mode where the number of photoelectrons per MeV detected by the photodetector is somewhat less, but still sufficient to achieve a statistical term in the resolution of 0.4-0.6%$/\sqrt{E}$(GeV). The specifications for the light output and performance for each type of crystal, along with their mechanical tolerances, are given in the section 5.2.

The readout will utilize a low gain phototube with a gain of approximately 10^5. It would have a UV glass window in the case of CsI, or a quartz window in the case of BaF_2. Using a phototube with a diameter of 28 mm, and an air gap coupling to the crystal, which gives the most reliable and stable light connection, we have measured a yield of approximately 30-50 photoelectrons per MeV of deposited energy. The signals from the phototube would then be in the range of 2.5 mV to 2.5 V for an energy range of 5 MeV to 5 GeV per crystal. With an equal split of the signal between the ADC and TDC, this will result in an ADC sensitivity of about 0.2 MeV per channel. The present ADC design for PHENIX calls for an effective 15 bit ADC, providing sufficient dynamic range for the full energy range to be covered with the proposed detector.

Another possible readout option would be to utilize a lower gain readout device, such as a vacuum phototetrode, which would provide a gain of about 30, followed by a fast preamplifier and shaping amplifier to provide the additional gain. This would have the advantage of having a readout device for which the gain is less sensitive to voltage variations, in addition to making an independent calibration of the electronic gains possible.

For any of these options, the detector will achieve an energy resolution of better than $2\%/\sqrt{E(\mathrm{GeV})} \oplus 1\%$ with a low energy threshold of 1-2 MeV. The expected position resolution will be less than 4.5 $\mathrm{mm}/\sqrt{E(\mathrm{GeV})}$, and the time resolution will be in the 100 ps range or less, significantly better than what can be obtained with the Pb/scintillator or Pb-glass detectors.

Both BaF_2 and undoped CsI have been extensively studied in terms of their performance and ability to measure low energy photons. The test results of our CsI prototype detector, as well as preliminary results from our timing measurements with BaF_2, are discussed in section 5.3. A discussion of the results obtained with BaF_2 used in several actual experiments can be found in refs.[23] and [45]. The results clearly demonstrate that either undoped CsI or BaF_2 can meet the performance requirements of the proposed high resolution photon detector.

Crystals of approximately 17 radiation lengths depth would be required in order to maintain good energy resolution at higher energies, as discussed in Chapter 4. Undoped CsI crystals of this length are presently available from a number of western manufacturers [57], as well as from suppliers in the former Soviet Union [58]. High quality single crystals of BaF_2 in lengths up to 35 cm are currently being produced in China [59], and may also be available from the former Soviet Union [60]. Since the cost of either material is presently comparable, we consider both of these options to be on an essentially equal footing at this time. The final decision will be based on the performance of sample crystals of both types from the potential suppliers, and the respective pricing bids for the total of 3600 crystals.

5.2 Crystal Specifications

- Dimensions CsI crystal : 3.5 x 3.5 x 32 cm^3
- Dimensions BaF_2 crystal : 3.5 x 3.5 x 35 cm^3
- Mechanical tolerances : $\pm$ 0.005 inches ($\pm$ 0.13 mm) on all dimensions
- Polish : standard optical polish on all surfaces

- Optical quality : crystals shall be free of any cracks, chips or inclusions
- Optical transmission : crystals shall exhibit no discernable absorption bands in the 280-800 nm wavelength range for CsI, or 200-800 nm for BaF_2
- Light output : Light output shall be measured as the number of photoelectrons (p.e.) produced on a standard 2 inch diameter photomultiplier tube having a bialkali photocathode and UV glass window, or a quartz window for BaF_2. These energy measurements are typically carried out using gamma ray sources such as ^{137}Cs. The crystal shall be wrapped with 0.005 inches thick (0.13 mm) UV reflecting white teflon and 0.001 inches (0.03 mm) of aluminized mylar on all surfaces except the readout end, which will be coupled to the face of the photomultiplier tube with a UV transmitting optical grease. In the case of CsI, the light output shall be a minimum of 250 p.e. per MeV measured in a 100 ns integration time. For BaF_2, the number of photoelectrons shall be a minimum of 200 (1500) measured in an integration time of 20 ns (1 μs).
- Light output uniformity : The light output (L) shall not vary by more than 5% over the length of the crystal, defined by the ratio $(L_{max} - L_{min})$ / L_{ave}, over the distance from 2 cm to 30 cm from the readout end for CsI (2 cm to 33 cm for BaF_2).
- Fast/total ratio : The ratio of the light output measured in a 100 ns integration time (fast) to the light output measured in a 1 μs integration time (total) shall be greater than 0.8 throughout the entire volume of the crystal for CsI. For BaF_2, the ratio of the light output measured in a 20 ns integration time to that measured in 1 μs shall be greater than 0.13 throughout the entire crystal.

5.3 Calibration and Monitoring

The energy and time resolution of the detector will be maintained and monitored using a calibration scheme based on a nitrogen laser, as shown in Figure 5.1. It will include high precision monitoring of the laser output power pulse by pulse in order to maintain the stringent stability requirements on resolution. Light from the laser will be directed into an integrating sphere which will act as diffuser and beam splitter. The interior surface of the sphere will consist of a material highly reflective for UV photons and have several small ports for indirectly viewing the scattered light from the laser. One port will be viewed by a biplanar phototube which will monitor the light output of the laser. The biplanar phototube (e.g., the Hamamatsu R1328U) is a special type of vacuum photodiode designed to monitor laser light intensity. It is inherently stable with unity gain, and capable of delivering a very high instantaneous current pulse (up to 300 mA) directly into a 50 Ω load. It has has a peak quantum efficiency at about 340 nm, which is well matched to the 337 nm emission of the nitrogen laser, and has a rise time of 60 ps. It can therefore also be used as a trigger for timing calibration and monitoring the stability of the time of flight resolution of the calorimeter. Other ports of the integrating spheres will be equipped with fiber optics interfaces to provide light distribution to the calorimeter modules. The light will be transported on a system of large core ($\sim$ 0.6 mm) quartz fibers to each detector module, where it will be further split to provide a single small core fiber ($\sim$ 0.1 mm) to each detector element. However, due to the inefficiencies at the various optical connections, and limitations on the output power of a single laser, it may be possible that more than one independent laser system (possibly up to three) will be required to service all of the modules in the calorimeter.

Both absolute and periodic relative calibrations are preferably done with the entire detector assembled and in its final location. This automatically takes into account the effects of the environment where the detector has to operate (temperature, noise, background from other detectors, etc.) Furthermore, calibration must be repeated periodically to follow gain drifts, to check for changes after minor repairs, such as replacement of phototubes, etc.

Minimum ionizing particles, either from low multiplicity events, or from cosmic rays, can provide one point for an absolute energy calibration. The typical energy deposition of a minimum ionizing particle is about 180 MeV (see Chapter 5.4), which is at the low end of the required dynamic range of the detector. Since the error from calibrating the detector at a single point grows linearly with energy, a precision of $\sigma(E)/(E) = 0.18\%$ at the minimum ionizing peak would be required in order to maintain a resolution of $\sigma(E)/(E) = 1\%$ at 1 GeV. This implies the same precision in the variation of the path length of minimum ionizing particles within a crystal, or knowledge of the angle of indicence to better than $0.1°$. The situation improves if another, higher energy point is added from other particles from real events. This can come from identified electrons, which will be measured with a precision of $\Delta p/p$ on the order of 0.5% - 1.0% in the momentum range 150 MeV/c - 5 GeV/c by the PHENIX tracking system[51]. Alternately, one can use photons from reconstructed π^0 s in low multiplicity events.

However, both electrons and photons generate large showers (6-12 crystals hit, depending on energy), and it is only the energy of the entire cluster that

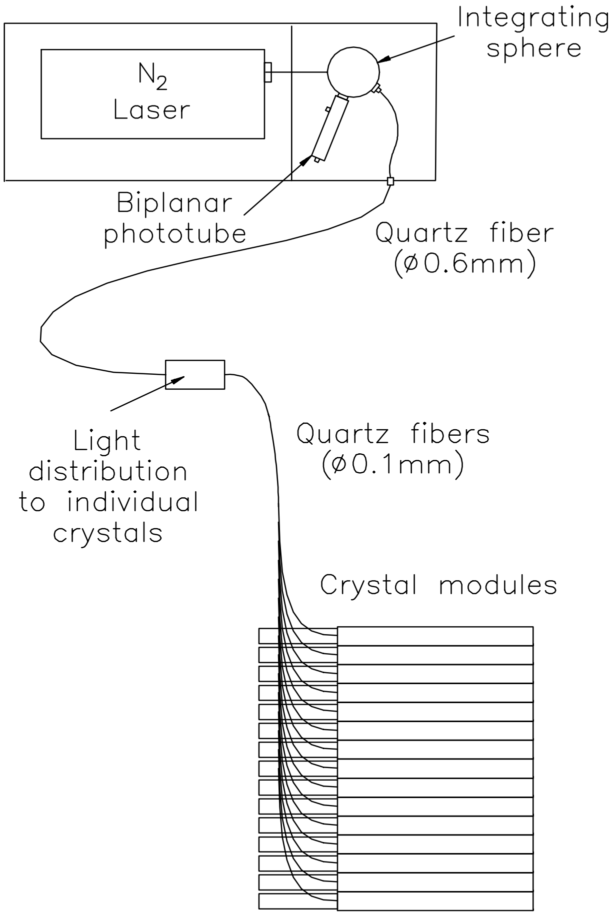

Figure 5.1: Laser based calibration system showing the light distribution to one module of the high resolution photon detector.

is known to high precision. An extension of the method proposed in [52] can be used to calibrate the individual crystals. If the energy E_c^j of the individual clusters in event j is known (electron case), and S_i^j is the signal measured in crystal i in event j, then the appropriate calibration constants c_i are those that minimize the expression

$$\sum_j (\sum_i c_i S_i^j - E_c^j) = \chi^2. \tag{5.1}$$

For photons, e.g. from π^0 decay, E_c is not known, and the above minimization must be performed with the additional constraint on the cluster energies E_1, E_2 and the opening angle θ :

$$m_{\pi^0}^2 = 2E_1E_2(1 - cos\theta). \tag{5.2}$$

If the higher energy calibration is taken around 1 GeV, the estimated time to obtain enough data to recalibrate all of the crystals would be a few weeks if the calibration events are obtained as downscaled peripheral triggers in Au+Au collisions. A dedicated run of a few hours at pp luminosities and with a photon trigger would be an alternative possibility.

5.4 Detailed Report on CsI Beam Tests

During the past two years, extensive laboratory and beam tests were performed with a prototype array of undoped CsI crystals. These studies focused on the following items:

- evaluation of the performance of crystals from different vendors.
- measurement of the energy and position resolution for electrons in the momentum range 0.05 - 6.0 GeV/c.
- determination of the hadron rejection capability (π/e separation).
- development of readout devices with high stability, fast timing, and good linearity over the full dynamic range expected at RHIC.
- a systematic study of calibration and monitoring of short and long term gain variations.
- a study of the timing resolution of undoped CsI and BaF_2 crystals.

The first prototype detector was built in 1991 and consisted of a 5×5 array of undoped CsI crystals, each measuring $3.5 \times 3.5 \times 30\,cm^3$. The transverse size was close to the Molière radius of CsI ($R_M = 3.8$ cm), and the length corresponded to 16.3 radiation lengths ($X_0 = 1.84$ cm). In 1992, the detector size was increased to 6×5, and a number of poor quality crystals were replaced with new, better quality crystals with higher light output. The crystals were wrapped in white reflecting teflon and aluminized mylar and placed inside a temperature controlled box. They were read out on one end with 1-1/8" diameter ten stage photomultiplier tubes (Hamamatsu R1398) which had a maximum gain of approximately 10^6. The phototubes were coupled to the crystals using only an air gap in order to maintain a high degree of reliability in the optical coupling, and because the light output of the crystals was sufficiently high (over 30 photoelectrons per MeV) that photostatistics did not contribute significantly to the overall energy resolution ($\leq 0.6\%/\sqrt{E}$).

The large dynamic range required at RHIC ($\approx$ 5 MeV - 5 GeV) requires that careful attention be paid to the linearity of phototube and readout system. For the beam tests described here, a relatively high gain phototube was used, and as a result, the voltage divider supplied by the manufacturer had to be substantially modified to provide a sufficiently linear response over the required range. Figure 5.2 shows the improvement in linearity over the standard design, indicating a linearity of better than 1% up to 40 mA, which corresponds to approximately 8 GeV per channel. The signals were read out using a 200 ns wide gate with a LeCroy 1885 FASTBUS dual range ADC, which provided effectively 15 bits of dynamic range. A separate "dummy" channel, consisting of a phototube inside the detector box which was not coupled to any crystal, but read out the same way as the other tubes, was used to check for channel to channel coherent noise correlations. Each crystal was individually calibrated using either the minimum ionization peak from high momentum pions, or the kinetic energy peak from low energy stopping pions. The gains were initially set to give a sensitivity of 1.4 MeV per ADC channel during the 1991 tests, but were later increased to 0.2 MeV per channel during the 1992 tests, corresponding to an upper limit of about 6.0 GeV/channel in the ADC.

A laser calibration system, similar to the one described in section 5.3, was added in 1992 in order to monitor short and long term gain variations. The system was based on a pulsed nitrogen laser (Laser Science VSL-337ND) operating at a frequency of 15 Hz. Light from the laser was distributed by a diffuser box to a 0.6 mm diameter quartz fiber which transported the light to the detector. Inside the detector, the light was split into individual 0.2 mm fibers which illuminated the back of each crystal which directed the light into each phototube. The output intensity of the laser varied by about 4 % from pulse to pulse and was monitored by a photodiode (a Hamamatsu R1328U biplanar phototube) which viewed the laser light directly from the diffuser box. The phototube gains were monitored using the ratio $R_i = C_i/D$, where C_i is the laser signal in the i-th channel and D is the signal in the photodiode for the same pulse. It was found that, although the response of the photodiode appeared to remain very stable over time, the ratio of the amount of light reaching the photodiode and that reaching the detector seemed to change by up to a few percent during the course of the beam tests. This was partly caused by slight changes in the position of the laser beam, and by a deterioration of the reflecting material inside the diffuser box. This limited the ability to monitor gain drifts to few percent. A new system, based on an integrating sphere as described in section 5.3, is currently being designed and should improve the overall gain monitoring capabilities to better than 1% over a period of several months.

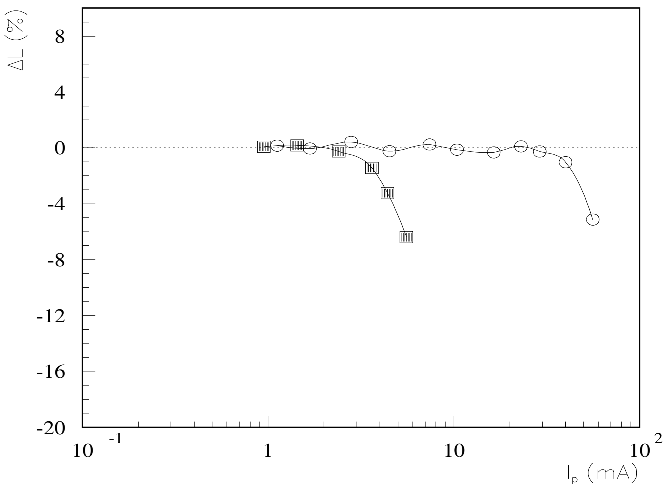

Figure 5.2: Phototube base linearity. Open circles show the linearity of bases modified for extended dynamic range, giving a nonlinearity of $\leq 1\%$ up to $40mA$ (≈ 8 GeV). Solid squares show the linearity of the factory supplied bases before modification.

5.4.1 AGS beam tests

The detector was tested in the C5 beamline of the Brookhaven AGS using a portion of the apparatus of the E814 spectrometer. This included a system of beam defining scintillators, two beam vertex detectors (BVER's) inside the vacuum beam pipe, a Čerenkov detector, a spectrometer magnet (D8), and a drift chamber (DCII) located 7 m downstream of the exit window of the beam pipe and just in front of the CsI detector. The CsI detector was mounted on a movable table for precise positioning in both the horizontal and vertical directions. The detector was tested with 1.0, 2.0 and 4.0 GeV/c beams of π^- and e^- during 1991, and with 1.0, 4.0 and 6.0 GeV/c beams of π^+, e^+ and protons during 1992.

Three types of triggers were used during the beam tests for data aquisition and monitoring: a random trigger to monitor pedestal shifts and to check noise correlations, a laser trigger to monitor the laser ratios, and a beam trigger for aquiring particle data. An event-by-event noise reduction scheme was implemented in the offline analysis to monitoring the pedestal shifts and noise correlations for every event. After all corrections, the noise on the sum of 3×3 crystals was 18 channels (3.8 MeV). The photomultiplier gains were equalized by an iterative online procedure which fitted the peak produced by minimum ionizing particles, and then adjusted the high voltage to set the peak into the same ADC channel for each crystal. In the subsequent offline analysis, using higher statistics, the gain correction factors g_i were equalized with greater accuracy, resulting in g_i factors which ranged from 0.98-1.03 ($\bar{g}_i =$ 1.003 and $\sigma_{g_i} = 0.018$). The laser ratios were constantly monitored during actual data taking and used to correct for gain drifts.

The momentum spread of the beam made a significant contribution to the apparent energy resolution in the CsI detector at all energies. However, this momentum spread was most difficult to correct for at lower energies because of multiple scattering of the beam in the material in front of the CsI detector, in particular, the beam scintillators, Čerenkov window, beam pipe window and air. For the 1992 tests, the beamline vacuum was extended up to the front of the spectrometer magnet, and a helium bag was installed inside the magnet which extended up to DCII in order to reduce multiple scattering in the air in front of the detector. Also, for part of the 1992 run, a second drift chamber (DCI) was placed at the entrance of D8 to help further improve the momentum resolution. However, as determined with data taken with no magnetic field, shown in the top right panel of Figure 5.3, the contribution of multiple scattering still accounted for about 2.3% in the energy resolution at 1 GeV. Unfolding this from the measured values of E/P corrected for the actual beam spread, which is shown in the lower right panel of Figure 5.3, gives an energy resolution of 2.1% at 1 GeV/c, as given in Table 5.1.

Extensive simulations have shown that the design goal of an energy resolution $\leq 2\%/\sqrt{E}$ can be maintained even if the shower energy is obtained from the sum of 3x3 crystals, as opposed to a 5x5 sum. This is important in order to cope with the high multiplicities and resulting high occupancies expected at RHIC. Therefore, in the analysis of the test beam data, the energy resolution was based on the energy measured in a 3x3 sum. The measured energy resolutions (including the resolution at the π^+ and p straight-through peaks) are summarized in Table 5.1 and shown in Figure 5.3 for 1.0 GeV/c. The width attributable to multiple scattering is subtracted quadratically except for the straight-through peaks, where the measured peak is approximately independent of particle momentum. Due to the low flux of electrons at higher momenta, along with the limited electron identification capability of the Čerenkov counter, the statistics for higher momentum electrons was very low. However, the higher energy electron data did show there was no noticeable nonlinearity in the detector and readout system at higher energies.

The shower position was computed using a logarithmic weighting procedure [61] where the calculated position, e.g., in the x direction is:

$$x_{calc} = \frac{\sum \omega_i x_i}{\sum \omega_i}, \qquad \omega_i = max\{0, W_0 + \ln(E_i/E_T)\} \tag{5.3}$$

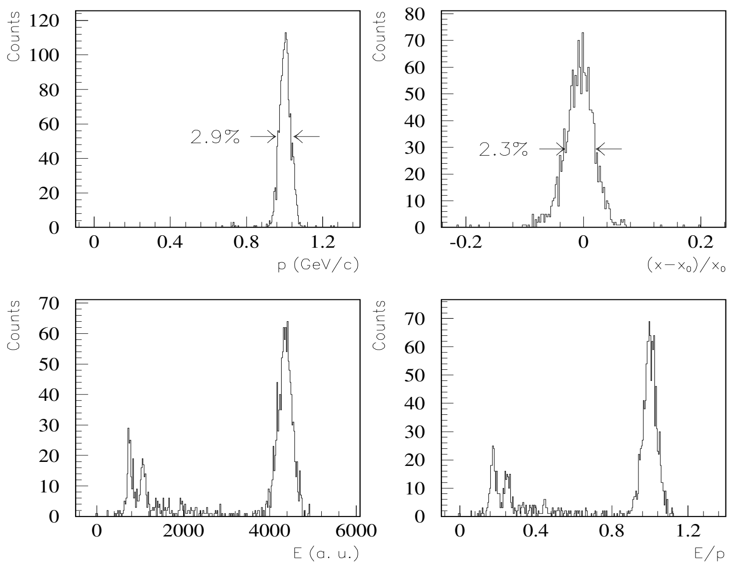

Figure 5.3: Results from the AGS tests in 1992 with a 1.0 GeV/c positive beam (π^+, e^+, p). Top left: beam momentum as determined from tracking (includes effect of multiple scattering). Top right: multiple scattering at zero field. Bottom left: energy in 3x3 crystals not corrected for beam momentum spread. Note that the p and π^+ straight-through peaks are clearly distinguishable. Bottom right: E/p ratio, corrected actual beam momentum spread, but uncorrected for the apparent momentum spread due to multiple scattering.

Table 5.1: Results from the 1992 tests at the AGS. Energy resolution $\sigma(E)/E$ for different particles species with nominal energy deposit E_{nom}.

Species	E_{nom} (GeV)	$\sigma(E)/E(\%)$
π^+	0.184	6.3
p	0.224	5.4
e^+	1.0	2.1

The summation goes over all crystals i, and E_T is the total energy. The free parameter W_0 serves as a threshold energy to cutoff channels where the noise is comparable to the deposited energy, and to minimize the contribution of shower fluctuations and noise. It was found that the optimal resolution could be obtained using a constant value of $W_0 = 3.7$ which was independent of energy. Comparison of the position obtained with the above method with the much more precise position measurement from the drift chamber DC II gave the position resolution of the detector. These results are listed in Table 5.2 for

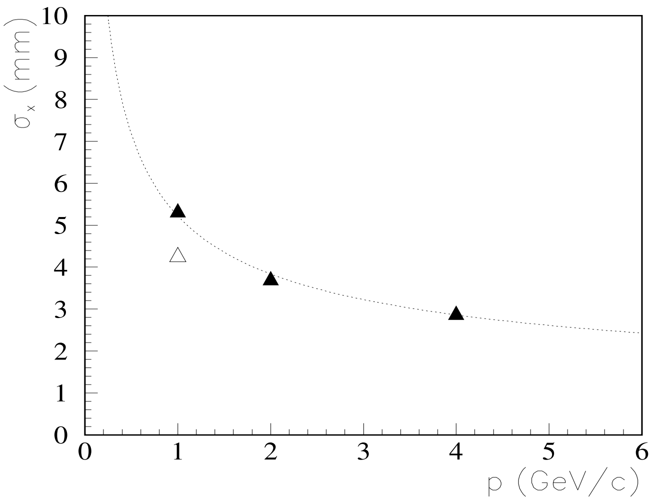

Figure 5.4: Position resolution σ_x (mm) for electrons as a function of beam momentum. Solid symbols: 1991 data. Open symbol: 1992. The dotted curve is a fit to the 1991 data (see text).

the 1991 run and shown in Figure 5.4. The position resolution for 1991 can be parameterized as:

$$\sigma_x = 0.5 + 4.7/\sqrt{E}(mm) \tag{5.4}$$

Although the position resolution was not measured at all energies in the 1992 run, the results showed a significant improvment at 1 GeV/c, as indicated in Figure 5.4. Assuming the same constant term as in the 1991 data, the statistical term would be $3.8/\sqrt{E}$ mm. At the proposed distance of 5.1 m from the intersection, this corresponds to an angular resolution of 0.056° for a 1 GeV photon.

The transverse shower size was also determined from the data and compared with Monte Carlo predictions. Figure 5.6 compares the transverse shower profile for 1 GeV electrons and interacting pions with showers simulated using GEANT. The results indicate again that agreement is quite good.

The π/e separation of the electromagnetic calorimeter is particularly important for the planned dielectron measurements in PHENIX, where the energy is measured in the calorimeter and the momentum is measured in the tracking devices in front of the photon detector. In the AGS beam tests, the electron identification and hadron rejection capability of the CsI detector was measured using the Čerenkov counter to select π^-'s and e^-'s in the beam, and the E814 spectrometer was used to measure the beam momentum. The

Table 5.2: Results from 1991 (AGS) and 1992 (TRIUMF) beam tests. Position resolution, π/e separation and electron efficiency as a function of beam momentum. For the low momentum points (TRIUMF, 1992) there was no independent beam position measurement.

p (GeV/c)	σ_x (mm)	π/e Sep.	e eff
0.1		1.1×10^{-2}	95 %
0.2		5.8×10^{-2}	95 %
0.3		8.9×10^{-2}	95 %
1.0	5.36	5.3×10^{-3}	97 %
2.0	3.74	2.1×10^{-3}	95 %
4.0	2.91	2.6×10^{-3}	93 %

π/e separation was determined by keeping the electron efficiency around 95% for different momenta in the range from 0.1-4.0 GeV/c. The results are given in Table 5.2, and the corresponding spectra for $p = 1.0$ GeV/c are shown on Figure 5.5. Note that the few surviving "pion" events are located just under the electron peak, and are most likely electrons which were misidentified due to the inefficiency of the Čerenkov detector. Therefore, the true π/e rejection of the CsI detector could actually be significantly higher. Also shown is the energy spectrum of pions in the detector simulated using GEANT. It is clear that the agreement between the shape of the real data and the simulated spectrum is quite good.

5.4.2 TRIUMF beam tests

In order to study the response to low momentum pions and electrons (down to 50 MeV/c), the detector was tested in the M11 beam at TRIUMF during August 1992. The tests were carried out with positive and negative beams of e's, π's and μ's at momenta of 50, 100, 200 and 300 MeV/c The momentum spread in the beam was $\leq 1\%$ for all momenta. Particles were identified using time of flight, and by measuring energy loss (dE/dx) in one of the beam scintillation counters. Signals were digitized using CAMAC 2249W (11 bit) ADCs, which have a factor of 5 lower resolution (0.25 pC/channel) than the LeCroy 1885 FASTBUS ADC's used in the AGS beam tests. In order to preserve the desired dynamic range, the same gain settings were employed as were used at the AGS, which corresponded to ≈ 1 MeV/channel in the 2249W ADC. Noise

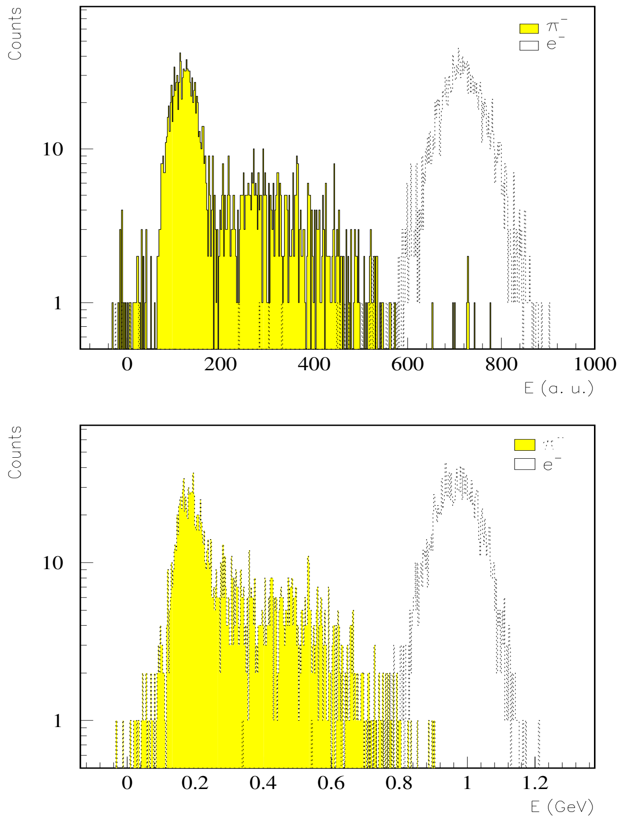

Figure 5.5: (a) Energy spectra for π^- and e^- with p = 1.0 GeV/c. The few surviving "pion" events at the electron peak are very likely result of an inefficiency in the Čerenkov detector. (b) Simulated energy spectrum for pions from GEANT

levels were found to be within the ADC resolution (typical $rms \approx 0.8 - 1.1$ channels), and no correlation was found between individual channels and the dummy channel. The rms noise for the 3x3 channel sum was 3.2 channels, corresponding to 3.2 MeV, and was comparable to the noise level (after noise correction) found in the AGS tests. Each crystal was calibrated using the the full kinetic energy peak (109 MeV) of p = 200 MeV/c positive pions which were stopped in the CsI detector, as shown in the lower left hand panel of Figure 5.7. The variance of the offline gain equalization factors compared to their values for the AGS tests was only 5.6%, showing that the calibration was remarkably stable and transportable.

Energy spectra for 50, 100, 200 and 300 MeV/c electrons and 200 MeV/c $\pi^\pm$ are shown in Figure 5.7. Since the showers spread out in only 2 - 7 crystals at this low energy, the total energy is obtained by adding up only those crystals

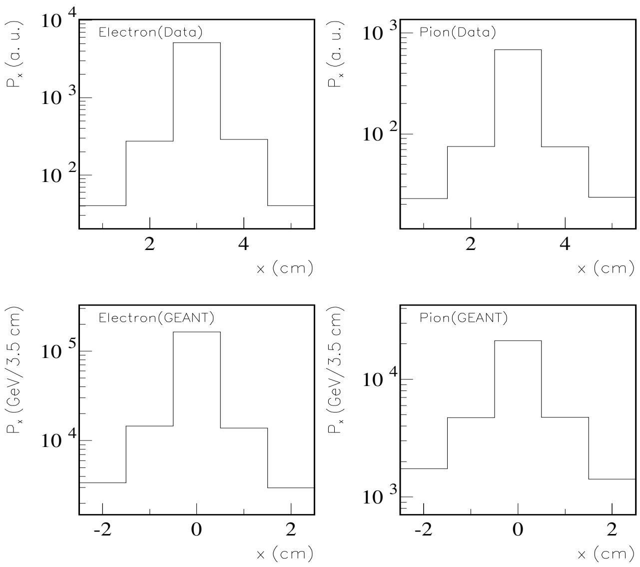

Figure 5.6: Transverse shower profile for 1 GeV showers (a) measured data (b) simulated using GEANT.

Table 5.3: Results from the 1992 tests at AGS and TRIUMF. Energy resolution for different momenta and particle species. Shower size (mean number of crystals with energy above 2.0 MeV) is also indicated. The last point (1 GeV) was from the 1992 AGS test.

p (MeV/c)	Species	$\sigma(E)$ (MeV)	$\sigma(E)/E$	$\sigma(E)/\sqrt{E(GeV)}$	Crystals hit
50	e^+	4.2	8.3%	1.9%	2.8
100	e^+	5.7	5.7%	1.8%	4.0
200	e^+	8.9	4.5%	2.0%	5.6
200	π^+	3.3	3.1%	1.0%	3.3
300	e^+	10.2	3.4%	1.9%	6.9
1000	e^+	21.2	2.1 %	2.1 %	10.8

that are above a certain energy threshold (2.6 MeV in this case) rather than summing the signal in a fixed number (3×3) of crystals. This procedure is similar to that which would be used in a clustering algorithm when analyzing physics data, and eliminates the additional noise contribution. The energy resolutions and the mean number of crystals with energy above the threshold are listed in Table 5.3 and plotted in Figure 5.8. The measured energy resolution

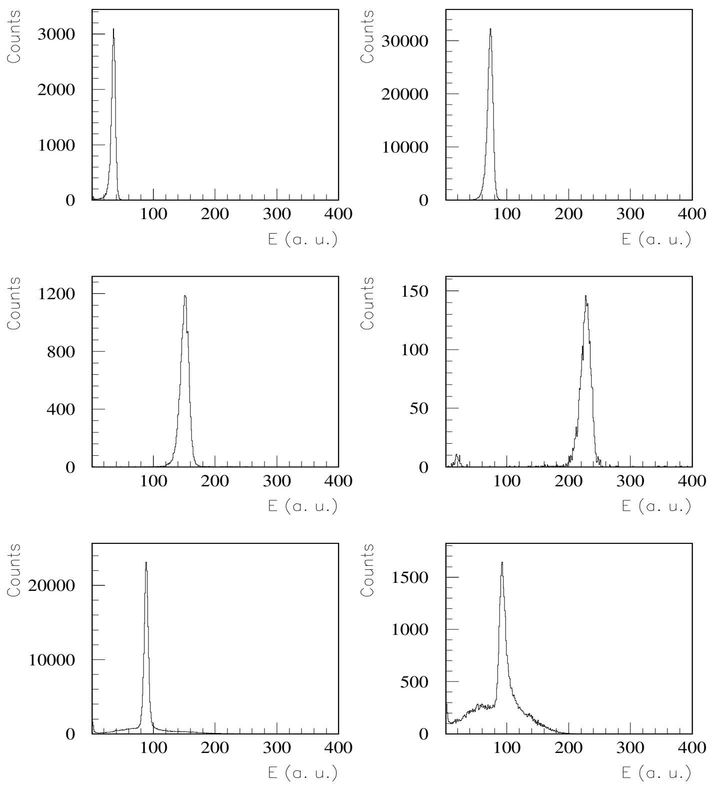

Figure 5.7: Response of the detector to low momentum particles measured at TRIUMF. Crystals with energy above a threshold of 2.0 MeV are summed. Top and center row: electrons of 50, 100, 200 and 300 MeV/c momentum, respectively. Bottom row, left panel: 200 MeV/c π^+. Bottom row, right panel: 200 MeV/c π^-.

can be parameterized as:

$$\frac{\sigma(E)}{E} = 0.8\% \oplus \frac{1.8\%}{\sqrt{E}} \oplus \frac{0.3\%}{E} \tag{5.5}$$

It should be noted that this final result is actually better than our design goal of $1\% \oplus 2\%/\sqrt{E}$.

The π/e separation was also measured at lower energies and is given in Table 5.2. Electrons and pions were identified using a combination of time of flight and dE/dx measurements in the beam defining scintillation counters. For an electron efficiency of 95%, the π/e separation was in the range on 1-9$\times10^{-2}$ for momenta between 100-300 MeV/c.

Since the light output of the crystals is quite high, a vacuum phototetrode

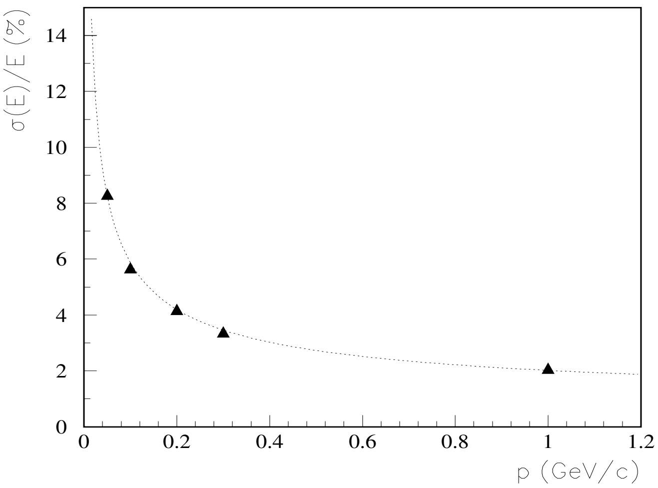

Figure 5.8: Resolution $\sigma(E)/E$ for electrons as a function of momentum in the range from 50 MeV/c to 1.0 GeV/c.

(Hamamatsu R2149) having a gain of ≈ 30 was also tested as a readout device. These devices offer the advantage of higher stability and linearity, and better ease of calibration. The phototetrodes were coupled to the crystals using RTV "cookies" to increase the light yield to ≈ 80 photoelectrons/MeV. The tetrodes were read out with custom designed preamplifiers and bipolar shaping amplifiers with a shaping time of ≈ 100 ns [62]. Measurements showed that with an appropriate gain setting, the noise level was ≈ 0.5 MeV/channel, which was partly due to pickup noise on the long cable that was amplified by the shaping amplifier. This contributed $\approx 0.64\%/E$ to the total energy resolution, and was approximately a factor two worse than the with the photomultiplier tubes. The overall energy resolution measured with the tetrode readout in the range from 50-300 MeV was:

$$\sigma(E)/E = 3.0\% \oplus 1.5\%/\sqrt{E} \oplus 0.6\%/E \tag{5.6}$$

The smaller statistical term is presumably due to the higher photostatistics, while the larger constant term is most likely due to larger gain variation factors and poorer gain balancing from channel to channel. Further improvements in reducing the noise are currently under way, as well as studies on the timing capabilities of the tetrode readout.

In March 1993, the timing resolution of undoped CsI crystals and BaF_2 crystals of the type that would be used in the actual detecotr was measured at TRIUMF. The tests were carried out in the M13 beam line which delivered a 150 MeV/c momentum positive beam of π^+, μ^+, and e^+. The beam was

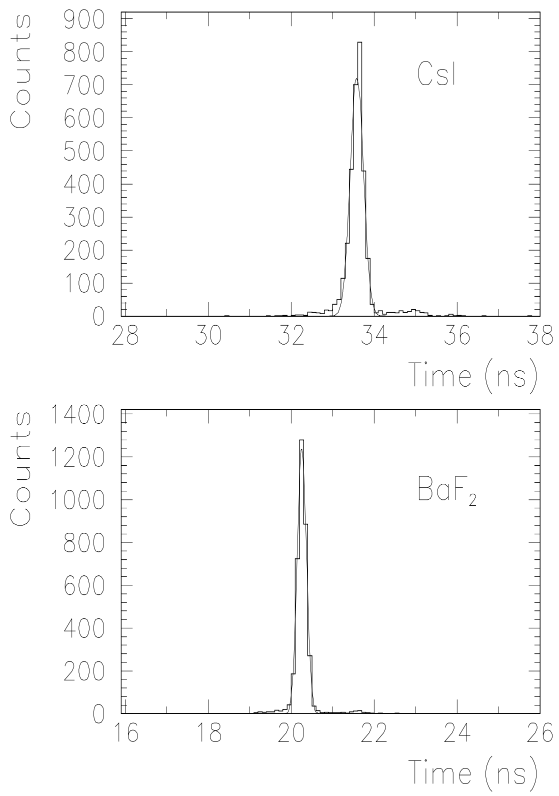

Figure 5.9: Timing resolution for 150 MeV/c electrons measured at TRIUMF. Top: CsI (σ = 159 ps). Bottom: BaF_2 (σ = 110 ps). After unfolding the 95 ps resolution of the start counter the numbers are 127 ps and 55 ps, respectively.

defined by two identical beam scintillators S1 and S2. S2 provided the start for the LeCroy 2228 TDC's which digitized the signals with a precision of 50 ps/count. Signals from the beam counters were discriminated with an Ortec 934 constant fraction discriminator, and signals dfrom the detector were digitized with either a similar 934, or a GSI CF 8001 CFD. The width of the time distribution for identified pions in S1, which constituted approximately 95 of the beam, was 135 ps. Since S1 and S2 were identical counters, we concluded that the resolution of the start counter itself was 95 ps.

For undoped CsI, our preliminary results are 159 ps, 130 ps and 128 ps for 150 MeV/c e, μ and π, respectively. These numbers include the resolution of the start counter. Unfolding the contribution of S2 results in 127 ps, 89 ps and 86 ps, respectively, for the three particle types.

For BaF_2 we measured 110 ps, 107 ps and 107 ps for e, μ and π before unfolding the contribution of the start counter. Correcting for the contribution of S2, the timing resolutions are 55 ps, 49 ps and 49 ps. In the BaF_2 case, the measurement was clearly limited by the timing resolution of the start counter and the resolution of the TDC. The results for both BaF_2 and CsI are shown in Figure 5.9.

Chapter 6

Costs and Schedule

A cost breakdown of the high resolution detector is given in Table 6.1. The final cost assumes the use of undoped CsI crystals produced at a price of \$3.50/cc and BaF_2 at a price of \$3.00/cc. Based on recent orders for CsI [63][64], these crystals could be supplied by western manufacturers at this price [57]. It is also possible that high quality undoped CsI may become available from manufacturers in the former Soviet Union [58]. The cost of the crystals in the case of the BaF_2 option is given assuming that the crystals would be produced in China [59]. For both options, it is assumed that the transverse dimensions of the crystals are 3.5×3.5 cm^2 and the length is approximately 17 radiation lengths (32 cm in the case of CsI and 35 cm for BaF_2). For the CsI option, the price for the readout includes a low gain, UV glass window phototube supplied by western manufacturers, while for the BaF_2 option, the cost is for quartz window phototubes. The total cost of the detector is about \$7.1M for both options.

The time scale for construction and installation of the high resolution detector into PHENIX will be determined primarily by the delivery schedule for the crystals. The detailed delivery schedule will be specified in a memorandum of understanding with the selected supplier, but is expected to take approximately three years from the start of production. For CsI, this is based on existing capacity with western suppliers. The production capability for producing BaF_2 crystals which meet the specified requirements, in sufficient quantities to meet our needs, can readily be met in China, and is presently being developed for both CsI and BaF_2 in the former Soviet Union. If production of the crystals were to start by the fall of 1993, we would expect all of the crystal modules to be completed by late 1996. This would be followed by installation in the calorimeter walls during the early part of 1997 and approximately nine month of in-situ testing and calibration before the start of

RHIC operation.

Item	Component item	Units	Unit cost ($)	Subtotal (k$)	Total (k$)
Materials CsI option					6900
(BaF_2 option)					(6951)
CsI crystals $3.50/cc		3600	1372	4939	4939
(BaF_2 crystals $3.00/cc)		3600	(1286)	(4630)	(4630)
UV PMT		3600	365	1314	1314
(Quartz PMT)		3600	(465)	(1674)	(1674)
	UV glass PMT's	3600	250	900	
	(Quartz PMT's)	3600	(350)	(1260)	
	Resistive bases	3600	95	342	
	Mu metal shields	3600	20	72	
HV Distribution		3600	100	360	360
Front end electronics		2000	46	92	92
Cables & connectors		2000	40	80	80
Monitoring system		3	13000	39	39
	Laser	1	6000	6	
	Biplanar PMT	1	2000	2	
	Integrating sphere	1	2000	2	
	Box & hardware	1	1000	1	
	Quartz fibers	bndl	2000	2	
Support structure		1	76000	76	76
	Mechanical support	1	60000	60	
	Temp. stabilization	sys	16000	16	
Testing and QA		24 mo	3000	72	72
	QA testing of crystals	12 mo	3000	36	
	QA testing of PMTs	6 mo	3000	18	
	Laser system testing	6 mo	3000	18	
Assembly & installation		12 mo	3000	36	36
EDIA		22 mo		130	130
	Engineer (mechanical)	6 mo	6400	38.5	
	Engineer (electrical)	6 mo	6400	38.5	
	Designer (mechanical)	6 mo	5300	32	
	Designer (electrical)	4 mo	5300	21	
Total (CsI option)					7138
Total (BaF_2 option)					(7189)

Table 6.1: Cost Estimate for High Resolution Photon Detector

Bibliography

[1] PHENIX Conceptual Design Report, BNL, January 1993.

[2] J. Huston, Proc. 1989 Int. Symposium on Lepton and Photon Interaction at High Energies, ed. M. Riordan (World Scientific, Singapore, 1990) p. 348.

[3] A. Angelis *et al.*, Phys. Lett. **B94**, 106(1980); M. Diakonou *et al.*, Phys. Lett. **B91**, 296(1980); E. Anassontzis *et al.*, Z. Physik **C13**, 277(1982); T. Akesson *et al.*, Phys. Lett. **B158**, 282(1985); A. Angelis *et al.*, Nucl. Phys. **B327**, 541(1989); T. Akesson *et al.*, Sov. J. Nucl. Phys. **51**, 836(1990).

[4] J. Badier *et al.*, Z. Physik **C31**, 341(1986); C. De Marzo *et al.*, Phys. Rev. **D36**, 8(1987); M. Bonesini *et al.*, Z. Physik **C38**, 371(1988).

[5] M. McLaughlin *et al.*, Phys. Rev. Lett. **51**, 971(1983); G. Alverson *et al.*, Phys. Rev. Lett. **68**, 2584(1992).

[6] T. Akesson *et al.*, Phys. Lett. **B158**, 282(1985); A. Bernasconi *et al.*, Phys. Lett **B206**, 163(1988); R. Ansari *et al.*, Z. Physik **C41**, 395(1988); F. Abe *et al.*, Phys. Rev. Lett. **68**, 2734(1992); R.E. Ansorge *et al.*, Z. Physik **C43**, 75(1989); C. Alvajar *et al.*, Phys. Lett. **B209**, 385(1988).

[7] J. Morfin and W. Tung, Z. Physik **C52**, 13(1991); A. Martin, W. Stirling and R. Roberts, preprint RAL-92-021, May 1992; W. Stirling, Proc. Joint Int. Lepton Photon Symposium & Europhysics Conference on High Energy Physics, ed. S. Hegarty, K. Potter and E. Quercigh (World Scientific, Singapore, 1992) p. 162.

[8] P. Braun-Munzinger and G. David, Proc. Int. Workshop on Gross Properties of Nuclei and Nuclear Excitations XX, Hirschegg, Austria, ed. H. Feldmeier (ISSN 0720-8715, Darmstadt, 1992) p. 8.

[9] P.V. Ruuskanen, in Proc. Quark Matter '91 Conference, Gatlinburg, TN, Nov. 1991, Nucl. Phys. **A544**, 169c(1992).

[10] G. Bertsch *et al.*, Phys. Rev. **D37**, 1202(1988).

[11] J. Kapusta *et al.*, Phys. Rev. **D44**, 2774(1991).

[12] M. Kataja, J. Letessier, P.V. Ruuskanen, and A. Tounsi, Z. Physik **C55**, 153(1992).

[13] C. Albajar *et al.*, UA1 collaboration, Nucl. Phys. **B335**, 261(1990).

[14] R. Albrecht *et al.*, WA80 collaboration, Z. Physik **C51**, 1(1991).

[15] D.K. Srivastava, B. Sinha, M. Gyulassy and X.N. Wang, Phys. Lett. **B276**, 285(1992).

[16] K. Geiger and J.I. Kapusta, Minneapolis Preprint, Oct. 1992.

[17] E.V. Shuryak, Phys. Rev. Lett. **68**, 3270(1992).

[18] E. Shuryak and L. Xiong, Phys. Rev. Lett. **70**, 2241(1993)

[19] L. Xiong, E. Shuryak, and G. Brown, Phys. Rev. **D46**, 3798(1992).

[20] E.V.Shuryak, Phys. Rev. **D42**, 1764(1990).

[21] E.V.Shuryak, Phys. Lett. **B231**, 175(1989).

[22] F.E. Low, Phys. Rev. **110**, 974(1958).

[23] C.Erd, Ph.D. Thesis, Technical University of Vienna, September 1991 (paper to be submitted to Z. Physik C).

[24] P.V. Chliapnikov *et al.*, Phys. Lett. **B141**, 276(1984).

[25] J.J. Aubert *et al.*, EMC Collaboration, Phys. Lett. **B218**, 248(1989).

[26] J.D. Bjorken and H. Weisberg, Phys. Rev. **D13**, 1405(1976).

[27] U. Görlach for the Helios Collaboration, Proc. Quark Matter '91 Conference, Gatlinburg, TN, Nov. 1991, Nucl. Phys. **A544**, 109c(1992).

[28] BNL AGS Experiment 855, Preliminary results, private communication C. Woody.

[29] F. Botterweck *et al.*, Z. Physik **C51**, 541(1991).

[30] S. Pratt, Phys. Lett. **B301**, 159(1993).

[31] F. Wilczek, Invited Talk, AGS and RHIC Users Meeting, BNL, 1992.

[32] J.L. Cortes and B. Pire, Phys. Rev. **D38**, 3586(1988).

[33] Z. Kunszt, Phys. Lett. **B218**, 243(1988).

[34] M.A. Doncheski and R.W. Robinett, Phys. Lett. **B248**, 188(1990).

[35] R.W. Robinett, Phys. Rev. **D43**, 113(1991).

[36] J. Ashman *et al.*, Phys. Lett. **B206**, 364(1988).

[37] C. Baglin *et al.*, Na38 Collaboration, Phys. Lett. **B262**, 362(1991).

[38] L. Antoniazzi, E705 Collaboration, Phys. Rev. Lett. **70**, 383(1993).

[39] T. Ferbel and W.R. Molzon, Rev. Mod. Phys. **56**, 18(1984).

[40] F. Binon *et al.*, NA12 Collaboration, Nucl. Instr. and Methods **A248**, 86(1986).

[41] WA98 Proposal, CERN/SPSLC 91-17, May 1991.

[42] T.K. Hemmick in PHENIX Tech. Note 7, QM91 CDG Meeting, BNL Nov. 1991

[43] The CLEO II CsI electromagnetic calorimeter at Cornell.

[44] The L3 BGO electromagnetic calorimeter at CERN.

[45] R. Novotny, IEEE Trans. in Nucl. Sci. **38**, 379(1991).

[46] T. Awes, P. Braun-Munzinger *et al.*, Recommendations Concerning a Technology Choice for the PHENIX Electromagnetic Calorimeter, PHENIX Tech. Note 64, BNL Nov. 1992

[47] F. Berger *et al.*, preprint IKP-MS-92/0102, submitted to Nucl. Instr. and Methods.

[48] E. Longo and I. Sestili, Nucl. Instr. and Methods **128**, 283(1975).

[49] U. Amaldi, Physica Scripta **23**, 409(1981).

[50] C. Fabjan and T. Ludlam, Ann. Rev. Nucl. Part. Sci **32**, 335(1982).

[51] PHENIX Experiment at RHIC; Preliminary Conceptual Design Report, BNL, June 1992.

[52] FERMILAB, E774 proposal.

[53] G. David, private communication.

[54] R. Sternheimer, Phys. Rev **99**, 277(1955).

[55] G.E. Kopylov, Nucl. Phys. **52**, 126(1973); J. Antos, Nucl. Instr. and Methods **A249**, 241(1986).

[56] A. Shor and R. Longacre, Phys. Lett. **B218**, 100(1989).

[57] Western suppliers of undoped CsI include: Quartz and Silice, France; CRYSTRAN, a division of Merck, U.K.; Horiba, Japan.

[58] CsI from the former Soviet Union is available from the Institute for Single Crystals, Kharkov, Ukraine.

[59] BaF_2 from China is available from the Beijing Glass Research Institute and the Shanghai Institute of Ceramics.

[60] BaF_2 from the former Soviet Union is available from the St. Petersburg Optical Physics Institute, St. Petersburg, Russia.

[61] T.C. Awes *et al.*, Nucl. Instr. and Methods **A311**, 130(1992).

[62] Z.Sobolewski, Syracuse University, 'Generic R&D on Undoped Cesium Iodide and Lead Fluoride', Proceedings of the Symposium on RHIC Detector R&D, BNL 52321, October 10-11,1991.

[63] CsI electromagnetic calorimeter for the KTEV experiment at Fermilab.

[64] CsI endcap photon veto detectors for experiment E787 at Brookhaven.